

**Characterization of Fluid Flow and Heat Exchange Heterogeneity  
in Natural and Synthetic Rock Fractures**

by

Noah A. Vriese

A thesis submitted in partial fulfillment of  
the requirements for the degree of

Master of Science  
(Geoscience)

at the

UNIVERSITY OF WISCONSIN – MADISON

2020

# Abstract

Quantitative studies of flow in fractured rock are important to engineering, hydrogeological, and geotechnical practices due to the ubiquitous nature of fractures in geological media. Importantly, fluid flow through fractured systems induces energy and chemical exchange with the host rock. The nature and magnitude of this exchange, however, is shown to be dependent upon several factors including flow path tortuosity and aperture heterogeneity. Due to the difficulty of observing flow fields in a natural fracture system, many studies of single-fracture flow rely upon geometric simplifications such as the parallel plate model. These models, however, lead to inaccuracies when predicting advection and diffusion in natural systems characterized by surface roughness, aperture heterogeneity, and flow channeling. While such deviations from parallel plate flow have significant effects on heat exchange characteristics within fractures, studies in this regard are lacking. To address this deficiency, this study is conducted to quantitatively model the effect of natural fracture variability on fluid flow and energy exchange processes. Natural fracture aperture geometries are acquired using white light interferometry for the purpose of numerical experimentation. Steady-state modeling of coupled heat diffusion and advection processes through the acquired fracture geometries is then conducted using COMSOL Multiphysics®. Parameters of interest include fracture surface roughness, aperture heterogeneity, flow anisotropy, and heat flux from the host rock to the fracture aperture during flow. Results suggest that surface roughness correlates with a reduction in hydraulic aperture and heat exchange efficiency. Additionally, it is observed that the spatial correlation of the aperture distribution is linked to heat exchange efficiency in heterogeneous fractures. Results from numerical modeling are corroborated with an established analytical solution.

# Acknowledgements

I would like to express my gratitude to my advisor Michael Cardiff for sharing his guidance and expertise through the wide range of topics examined in this study. I would also like to thank the members of the UW-Madison hydrogeology group for their helpful insights, camaraderie, and contagious enthusiasm for research.

I would like to acknowledge those who provided generous funding and equipment access which allowed this study to proceed. Portions of this work were funded by NSF Award #1654649 - CAREER: “Understanding transport processes in fractured sedimentary rock through multi-frequency and multi-method investigations”. Additionally, I would like to thank Dr. Sone, and Dr. Zoet for their technical support, and for use of their laboratory apparatus for critical aspects of this work.

I am grateful to have had the opportunity to take courses at both Michigan State and UW-Madison. I would like to thank all the faculty who contributed their time and effort to impart their expertise. I would like to especially thank those who gave me early opportunities to conduct research, namely Dr. Rooney, Dr. Schrenk, and Dr. Zarnetske. Thank you all for your belief in my abilities, mentorship, knowledge, and inspiration.

I know that any arduous journey is made better with the companionship of others. In this regard I would like to thank all the current geoscience graduate students with whom many laughs, and insightful conversations have been shared. Additionally, I would like to thank my fiancé Monica for her ever-present support through the ups and downs of both undergraduate and graduate study.

This thesis represents the culmination of not just the last two years of study, but rather a lifetime of support from some very special people. I would like to thank my parents for their relentless optimism and belief in my abilities. I certainly would have never made it this far without your help.

## TABLE OF CONTENTS

<b>Abstract .....</b>	<b>i</b>
<b>Acknowledgements .....</b>	<b>ii</b>
<b>LIST OF FIGURES.....</b>	<b>v</b>
<b>LIST OF TABLES.....</b>	<b>viii</b>
<b>1. INTRODUCTION.....</b>	<b>1</b>
1.1. <i>Purpose and Scope.....</i>	1
1.2. <i>Importance of Fractures in Hydrogeology .....</i>	2
1.3. <i>Properties and Characterization of Natural Rock Fractures: A Brief Review .....</i>	3
1.4. <i>Flow in Individual Fractures: A Brief Review .....</i>	11
1.5. <i>Heat Transfer Mechanisms in Fractured Rock: A Brief Review .....</i>	17
1.6. <i>Solutions to Heat Transport in Fractured Rock: A Brief Review .....</i>	19
1.7. <i>Point of the Current Contribution .....</i>	25
<b>2. DEVELOPMENT &amp; CHARACTERIZATION OF NATURAL ROCK FRACTURES.....</b>	<b>27</b>
2.1. <i>Sample Selection and Preparation.....</i>	27
2.2. <i>Natural Fracture Surface Acquisition.....</i>	28
2.3. <i>Natural Aperture Composition.....</i>	29
2.4. <i>Fracture Spatial Statistics .....</i>	30
2.5. <i>Tables.....</i>	35
2.6. <i>Figures .....</i>	38

<b>3. SIMULATION OF FLOW &amp; HEAT EXCHANGE IN NATURAL &amp; SYNTHETIC ROCK FRACTURES .....</b>	<b>39</b>
3.1. <i>Modeling Software</i> .....	39
3.2. <i>Synthetic Fracture Surface &amp; Aperture Composition</i> .....	40
3.3. <i>Model Geometry</i> .....	42
3.4. <i>Physics and Boundary Conditions</i> .....	43
3.5. <i>Model Computational Scheme</i> .....	47
3.6. <i>Output Processing</i> .....	48
3.7. <i>Tables</i> .....	49
3.8. <i>Figures</i> .....	51
<b>4. RESULTS.....</b>	<b>53</b>
4.1. <i>Model Output</i> .....	53
4.2. <i>Analysis of Results</i> .....	55
4.3. <i>Primary Findings</i> .....	60
4.4. <i>Tables</i> .....	62
4.5. <i>Figures</i> .....	64
<b>5. CONCLUSIONS AND FUTURE WORK.....</b>	<b>74</b>
5.1. <i>Conclusions</i> .....	74
5.2. <i>Future Work</i> .....	75
<b>Bibliography .....</b>	<b>76</b>

# LIST OF FIGURES

FIGURE 1.1. THREE VARIABLE TOPOGRAPHIC TRANSECTS WITH EQUAL ROOT-MEAN-SQUARE ROUGHNESS (SHOWN HERE $S_q$ ) ILLUSTRATING THE DISADVANTAGE OF 1-DIMENSIONAL STATISTICAL METRICS. THE RIGHTMOST TRANSECT ILLUSTRATES THE LENGTH-DEPENDENCE OF ROOT-MEAN-SQUARE ROUGHNESS (FROM [10]).....	4
FIGURE 1.2. LOG-LOG PLOT OF A SURFACE TRANSECT POWER SPECTRAL DENSITY $P(k)$ AS A FUNCTION OF SPATIAL WAVENUMBER $k$ . A LINEAR SELF-AFFINE FRACTAL MODEL IS FIT TO THE SURFACE SPECTRUM. THE MODEL IS DESCRIBED USING TWO PARAMETERS A (SLOPE) AND $\log_{10}(C)$ (INTERCEPT) (FROM [7]). .....	6
FIGURE 1.3. SURFACE PROFILE WITH VARIABLE HURST EXPONENT $H$ .....	7
FIGURE 1.4. A TYPICAL SEMI-VARIOGRAM, DISPLAYING THE NUGGET, SILL AND RANGE (FROM [9])......	9
FIGURE 1.5. CROSS-SECTION OF THE ANALYTICAL MODEL DEVELOPED BY BÖDVARSSON AND TSANG 1982, [31]. .....	20
FIGURE 1.6. A BASIC SECTION OF THE FRACTURE SYSTEM CONSIDERED IN FIGURE 1.5 (FROM [31]). .....	21
FIGURE 1.7. STOCHASTIC DISCRETE FRACTURE NETWORK GENERATION USING THE GEOFRAC <sup>®</sup> MODEL. (FROM [2]) (A) PRIMARY STOCHASTIC PROCESS: POISSON PLANE GENERATION. (B) SECONDARY STOCHASTIC PROCESS: POISSON-VORONOI TESSELLATION OF PLANES. (C) TERTIARY STOCHASTIC PROCESS: RANDOM TRANSLATION AND ROTATION OF POLYGONS.....	23
FIGURE 2.1. ANALYSIS OF APERTURE FIELDS GENERATED USING NATURAL ( $H = 0.93_{\text{HET}}$ ), AND SYNTHETIC ( $H = 0.90_{\text{HET}}, H = 0.75_{\text{HET}}$ ) SURFACES SUBJECT TO 1.5 MM OF RELATIVE SHEARING IN THE X-DIRECTION. .....	38
FIGURE 3.1: COMPOSITE IMAGE OF THE COMSOL <sup>®</sup> FRACTURE MODEL CONTAINING THE $H=0.90$ SYNTHETIC FRACTURE. A. GRANITE DOMAIN WITH DIFFUSIVE-ONLY TRANSPORT, WITH FRONT AND BACK FACES REMOVED FOR VISIBILITY OF FRACTURE; B. FRACTURE DOMAIN WITH ADVECTIVE-DIFFUSIVE TRANSPORT AND CREEPING FLOW. .....	51
FIGURE 3.2 A-F. COMPOSITE IMAGE OF THE 1.5 MM SHEARED $H = 0.90$ COMSOL <sup>®</sup> FRACTURE MODEL WITH DIMENSIONS AND PHYSICS FOR REFERENCE. FIVE OTHER COMSOL <sup>®</sup> MODELS WERE MADE, NOT SHOWN, FOR THE CASES OF SHEARED AND NON-SHEARED $H = 0.75, 0.90$ , AND $H \approx 0.93$ (NATURAL) FRACTURE SURFACE ROUGHNESS (TABLE 3.2). NOTE THE 90° ROTATED ORIENTATION OF (A) FOR VISUALIZATION. ....	52

FIGURE 4.1 A,B. STREAMLINES SOLVED VIA STOKES FLOW (LEFT) IN 1.5 MM SHEAR DISPLACED  $H = 0.75_{\text{HET}}$  APERTURE FOR VARIABLE FLOW ORIENTATIONS. STREAMLINES ARE SUPERIMPOSED UPON APERTURE WIDTH DISTRIBUTION [MM]. STREAMLINE THICKNESS

IS PROPORTINAL TO FLOW VELOCITY. PRESSURE ISOBARS SHOWN (RIGHT) ILLUSTRATING LOCAL PRESSURE GRADIENT [PA]. 64

FIGURE 4.2 A,B. STREAMLINES SOLVED VIA STOKES FLOW (LEFT) IN 1.5 MM SHEAR DISPLACED  $H = 0.90_{\text{HET}}$  APERTURE FOR VARIABLE FLOW ORIENTATIONS. STREAMLINES ARE SUPERIMPOSED UPON APERTURE WIDTH DISTRIBUTION [MM]. STREAMLINE THICKNESS

IS PROPORTINAL TO FLOW VELOCITY. PRESSURE ISOBARS SHOWN (RIGHT) ILLUSTRATING LOCAL PRESSURE GRADIENT [PA]. 65

FIGURE 4.3 A,B. STREAMLINES SOLVED VIA STOKES FLOW (LEFT) IN 1.5 MM SHEAR DISPLACED NATURAL  $H = 0.93_{\text{HET}}$  APERTURE FOR VARIABLE FLOW ORIENTATIONS. STREAMLINES ARE SUPERIMPOSED UPON APERTURE WIDTH DISTRIBUTION [MM]. STREAMLINE THICKNESS

IS PROPORTINAL TO FLOW VELOCITY. PRESSURE ISOBARS SHOWN (RIGHT) ILLUSTRATING LOCAL PRESSURE GRADIENT [PA]. 66

FIGURE 4.4 A-F. HEAT FLUX MAGNITUDE ACROSS FRACTURE INTERFACE [ $\text{W}/\text{m}^2$ ] MEASURED FOR 1.5 MM SHEAR DISPLACED  $H = 0.75_{\text{HET}}$  MODEL AT VARIABLE FLOW ORIENTATIONS AND INLET VELOCITIES..... 67

FIGURE 4.5 A-F. HEAT FLUX MAGNITUDE ACROSS FRACTURE INTERFACE [ $\text{W}/\text{m}^2$ ] MEASURED FOR 1.5 MM SHEAR DISPLACED  $H = 0.90_{\text{HET}}$  MODEL AT VARIABLE FLOW ORIENTATIONS AND INLET VELOCITIES..... 68

FIGURE 4.6 A-F. HEAT FLUX MAGNITUDE ACROSS FRACTURE INTERFACE [ $\text{W}/\text{m}^2$ ] MEASURED FOR 1.5 MM SHEAR DISPLACED NATURAL  $H \approx 0.93_{\text{HET}}$  MODEL AT VARIABLE FLOW ORIENTATIONS AND INLET VELOCITIES..... 69

FIGURE 4.7 COMPARISON OF NUMERICAL MODEL OUTLET TEMPERATURES WITH THE 1-DIMENSIONAL ANALYTICAL SOLUTION FOR FLOW BETWEEN PARALLEL PLATES. 'NUMERICAL PP SOLUTION' REFERS TO THE PARALLEL PLATE FEM MODEL BUILT IN COMSOL<sup>®</sup>. ALL MODELS ( $H = 0.75_{\text{HOM}}, 0.90_{\text{HOM}}, 0.93_{\text{HOM}}$ ) POSSESS A HOMOGENEOUS 0.5 MM MEAN APERTURE WIDTH, BUT SURFACES OF VARIABLE ROUGHNESS..... 70

FIGURE 4.8 A-B. PARALLEL PLATE-NORMALIZED FRACTURE SURFACE HEAT FLOW MAGNITUDES PLOTTED AS A FUNCTION OF FLOW PECLET NUMBER FOR THE 1.5 MM SHEAR-DISPLACED  $H = 0.75_{\text{HET}}, 0.90_{\text{HET}}$ , AND  $0.93_{\text{HET}}$  NATURAL SURFACE MODELS. DATA IS SHOWN FOR MODEL RUNS IN BOTH THE X AND Y-AXIS PARALLEL DIRECTIONS. IT IS OBSERVED THAT (1) VARIABILITY IN HEAT FLUX BETWEEN MODELS DECREASES WITH INCREASED PECLET NUMBER, (2) HEAT FLUX DECREASES WITH SURFACE ROUGHNESS ESPECIALLY AT LOW PECLET NUMBERS..... 71

FIGURE 4.9. MEAN FRACTURE SURFACE HEAT FLOW PLOTTED AS A FUNCTION OF FLOW PECLET NUMBER FOR THE $H = 0.75_{\text{HOM}}$ , $0.90_{\text{HOM}}$ , $0.93_{\text{HOM}}$ ROUGH-WALLED 0.5 MM APERTURE (RW) MODELS AND THE 0.5 MM APERTURE PARALLEL PLATE (PP) NUMERICAL MODEL .....	72
FIGURE 4.10 A-C. REPRESENTATIVE APERTURE CROSS SECTIONS ORIENTED PARALLEL TO FLOW FROM $H = 0.75_{\text{HOM}}$ , $0.90_{\text{HOM}}$ , $0.93_{\text{HOM}}$ MODELS SHOWING CALCULATED PECLET NUMBERS ( $\text{Pe}$ ) UNDER VARIABLE INLET VELOCITIES; FROM TOP TO BOTTOM $V_{\text{INLET}} = 0.1, 0.5, 1.0 \text{ CM/S}$ . IT IS OBSERVED THAT HIGH PECLET CHANNELS DEVELOP MORE FULLY WITH DECREASING ROUGHNESS. ALSO, DIFFUSIVE TRANSPORT IS SHOWN TO DOMINATE AT LOW PECLET NUMBERS. ....	72
FIGURE 4.11 A-C. ILLUSTRATION OF HEAT FLOW ANISOTROPY WITH FLOW DIRECTION AND RELATION TO APERTURE WIDTH CORRELATION LENGTH ( $\xi$ ). MEAN FRACTURE HEAT FLOW IS PLOTTED AS A FUNCTION OF FLOW PECLET NUMBER FOR 1.5 MM SHEAR-DISPLACED MODELS. IT IS OBSERVED THAT LONGER APERTURE WIDTH CORRELATION LENGTHS CORRELATE WITH ENHANCED HEAT FLOW ESPECIALLY AT PECLET NUMBERS $> 60$ . ....	73

# LIST OF TABLES

TABLE 2.1: TRIAXIAL TESTING RESULTS.....	35
TABLE 2.2: SCAN ACQUISITION PARAMETERS .....	35
TABLE 2.3. MEASURED FRACTURE SURFACE HURST EXPONENT ( $H$ ) FROM R/S AND PSD METHODS. MEASURED RMS ROUGHNESS ALSO REPORTED FOR REFERENCE. METHOD RMSE FROM $H$ MEASUREMENTS ON SYNTHETIC CALIBRATION SURFACES OF CONSTRAINED $H$ PRESENTED.....	36
TABLE 2.4. PARAMETERS USED TO GENERATE SYNTHETIC FRACTURE APERTURES.....	37
TABLE 2.5 APERTURES CREATED WITH NATURAL GRANITE WLI SURFACES WITH STANDARD STATISTICS DENOTED. SUBSCRIPT HOM REFERS TO HOMOGENEOUS APERTURE DUE TO NO FRACTURE SURFACE SHEAR, SUBSCRIPT HET REFERS TO HETEROGENEOUS APERTURES PRODUCED BY X-DIRECTION SURFACE SHEAR.....	37
TABLE 3.1. PARAMETERS AND BOUNDARY CONDITIONS UTILIZED IN COMSOL SIMULATIONS.....	49
TABLE 3.2. APERTURES USED FOR COMSOL MODELING WITH SURFACES IMPLEMENTED AND STANDARD STATISTICS DENOTED. SUBSCRIPT HOM REFERS TO HOMOGENEOUS APERTURE DUE TO NO FRACTURE SURFACE SHEAR, SUBSCRIPT HET REFERS TO HETEROGENEOUS APERTURES PRODUCED BY X-DIRECTION SURFACE SHEAR. ....	50
TABLE 4.1. NORMALIZED HYDRAULIC APERTURE, APERTURE WIDTH CORRELATION LENGTH, MEAN PECLET NUMBER, AND MEAN INTERFACE HEAT FLOW CALCULATED AT 1 CM/S INLET VELOCITY AND AVERAGED IN BOTH FLOW DIRECTIONS. NOTE: NATURAL SURFACE CORRESPONDS TO $H = 0.93$ MODELS.....	62
TABLE 4.2. COMPARISON OF ANALYTICAL AND NUMERICAL FRACTURE OUTLET TEMPERATURES FOR NUMERICAL MODEL VALIDATION. ROOT-MEAN-SQUARED-ERROR (RMSE) CALCULATED RELATIVE TO THE 'ANALYTICAL PARALLEL PLATE SOLUTION'. SEE FIGURE 4.7 FOR THE GRAPHICAL REPRESENTATION OF THIS DATA WITH THE ADDITION OF THE NUMERICAL ROUGH-WALLED HOMOGENEOUS APERTURE MODEL SOLUTION OUTPUTS. ....	63

# 1. Introduction

## 1.1. Purpose and Scope

Fractures are important in engineering, geotechnical, and hydrological work because they allow for the rapid transmission of fluids, energy, and contaminants through subsurface media. The scale of fractures can range considerably, with apertures spanning microns to centimeters, and typical lengths spanning centimeters to kilometers. However, because flow behaviors within natural fractures often possess significant heterogeneity and directional dependence, characterization is challenging even under laminar flow conditions. Furthermore, the direct observation of flow within fractures is difficult, which has led to a general oversimplification of fracture geometries and flow in modeling work. The heterogeneity of apertures formed from rough-walled fracture surfaces is often neglected, and approximated with a parallel plate geometry, thereby causing inaccuracies in flow and transport predictions. To address this, the work in this thesis investigates the effect of fracture surface roughness on aperture heterogeneity, flow, and heat exchange within a series of realistic aperture geometries. Through direct three-dimensional simulation the complex interactions of geometric, hydraulic, and thermal parameters may be visualized within a single fracture. The development of observable relationships between these characteristics within fractured rock has implications for field-scale applications such as improved production from enhanced geothermal systems.

## 1.2. Importance of Fractures in Hydrogeology

Flow and transport in geological media are often calculated assuming that geological formations are homogeneous. However, most natural subsurface geological media is fractured to some extent. Fractures within otherwise homogeneous porous media can significantly modify hydraulic behavior and, if oriented preferentially, can introduce flow anisotropy.

In the case of low-permeability formations, subsurface fluid flow occurs primarily through fracture networks [1]. It is on this basis that various fracture network models have been developed [2]. In these models the rock matrix is often assumed to be impermeable except for the fracture network, which is composed of fractures of uniform aperture. Flow velocity within these fractures is assumed to be uniform and derived from the cubic law (Eq. 1.11). However, more recent work has shown that these models are insufficient in replicating flow and transport in real systems due to the characteristic heterogeneity of individual natural fracture apertures [3].

Similarly, studies of solute transport through fractures and within fractured rock have historically relied upon solutions for flow derived from a uniform aperture geometry [4], [5]. In these solutions, flow is typically modeled through a one-dimensional constant aperture domain with a constant flow velocity derived from the cubic law, which is then coupled with a two-dimensional matrix diffusion model simulating transport in the host rock. While commonly used, these simplified systems neglect the effects of non-planar fracture faces on flow and contaminant transport behavior. More recent numerical studies have shown that rough-walled fractures, and their associated spatially variable apertures, significantly increase flow velocity heterogeneity, thus leading to complex solute/fluid dispersion and sorption behaviors [6].

Therefore, in order to accurately model the complex flow and transport behaviors within natural fracture systems, the fundamental problem of flow and transport within a rock body containing a realistic fracture must first be well understood. To accomplish this, a realistic and heterogeneous aperture geometry should be considered. This study is thus presented to investigate the effects of surface roughness and aperture heterogeneity on flow and transport within a series of three-dimensional rough-walled fractures.

### **1.3. Properties and Characterization of Natural Rock Fractures: A Brief Review**

Accurate description of surface roughness is critical to workers in a range of geotechnical and engineering disciplines. In geological materials, surface roughness affects frictional behavior, rock joint stiffness, fault zone evolution, and local fault stress distributions [7]. For workers in groundwater hydrology and petroleum systems analysis, surface roughness has been shown to control fluid flow behaviors from the fracture to reservoir scale [8]. The link between morphological and hydro-mechanical properties of rock fractures is the focus of many studies which aim to predict effective hydrological parameters from fracture surface and aperture characteristics [9]. This brief review focuses upon the methods implemented in these studies. The first portion discusses a few of the current techniques for surface roughness characterization. The second portion reviews the relevant geostatistical methods which are used in fracture surface and aperture characterization.

Despite technical improvements in recent years that allow for the acquisition of high-resolution spatial data, the quantitative characterization of fracture surface roughness remains

challenging. Most commonly, surface roughness is characterized using either statistical or spectral descriptions along a 1-dimensional cross section or profile. While relatively simple to implement, statistical measurements of surface roughness only address the aggregate variability of a surface, and are incapable of measuring spatial correlation. Additionally, commonly used statistical metrics such as the root-mean-square roughness ( $Rq$  or  $Sq$ ) (Eq. 1.1) or centerline roughness ( $Ra$ ) (Eq. 1.2) are often found to be dependent upon the length  $L$  of the topographic profile sampled:

$$Rq, Sq = \sqrt{\frac{1}{L} \int_0^L z^2(x) dx} \quad (1.1)$$

$$Ra = \frac{1}{L} \int_0^L |z(x)| dx \quad (1.2)$$

Where  $z(x)$  is the profile transect height as a function of position  $x$ . While these metrics provide some information about fracture roughness, in particular they do not capture information about spatial correlations in surfaces that may be important. For example, surfaces with dramatically different character may possess the same  $Rq$  or  $Ra$  as shown in Figure 1.1.

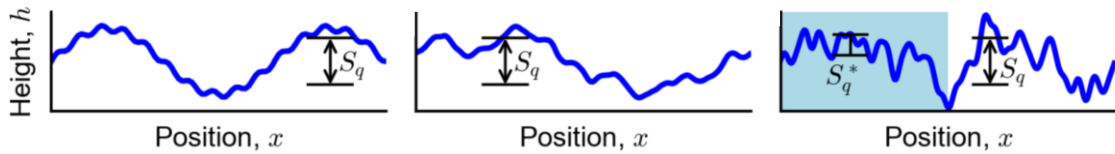


Figure 1.1. Three variable topographic transects with equal root-mean-square roughness (shown here  $Sq$ ) illustrating the disadvantage of 1-dimensional statistical metrics. The rightmost transect illustrates the length-dependence of root-mean-square roughness (From [10]).

Difficulties in the characterization of fracture surfaces over broad length scales using length-dependent statistical metrics have led researchers to devise measurement methods which are more scale-independent. Efforts to characterize the morphology of fracture surfaces using fractal models have found that natural fractures typically possess self-affine fractal properties regardless of the type of host rock or fracturing mechanism [11], [12]. Here self-affinity refers to the surface property in which a portion of a profile transect appears statistically the same as the whole profile if anisotropic magnification factors are used along its measurement axes. While few natural surfaces follow exact self-affine scaling, for many purposes self-affine fractal models provide a suitable description of natural surfaces. Because fractal models acknowledge the presence of roughness at all scales, they can be especially useful in describing natural fracture surfaces. Two parameter inputs  $\alpha$  and  $C$ , characterize a fractal model for a surface. The scaling exponent  $\alpha$  describes how the surface roughness changes with the scale of observation. Accordingly,  $\alpha$  may be used to describe the degree of self-affinity, while  $C$  is a measure of the topographic steepness or total profile variance at a given length scale (Eq. 1.3). These fractal roughness parameters can be estimated using spectral methods as discussed in the following.

Spectral measurements of surface roughness provide a robust and objective description based upon the frequency distribution of a profile. These approaches have been applied successfully by many authors in describing the roughness of both fractures and fault surfaces [13]. While there exist several spectral methods for roughness determination, this review will focus upon the Fourier power spectrum (FPS) method also known as the Power spectral density method (PSD) which may be used to estimate the scaling exponent  $\alpha$  for a 1-dimensional fracture profile [14]. The FPS method first requires the decomposition of a surface profile into

its one-sided frequency distribution via computation of the fast Fourier transform (FFT). The Fourier power spectrum  $P(k)$  is then calculated from the square of the amplitude of the Fourier transform as a function of spatial wavenumber  $k$ . Next, the Fourier power spectrum  $P(k)$  is normalized by the spatial wavenumber  $k$  to obtain the power spectral density (PSD). For a profile of length  $L$  containing  $N$  increments, the spatial frequencies range between  $1/L$  and the Nyquist frequency  $N/2L$ . When the PSD is plotted as a function of spatial wavenumber  $k$  in log-log space, a self-affine function exhibits a linear slope, which is proportional to the fractal scaling exponent  $\alpha$  (Figure 1.2. Eq. 1.3):

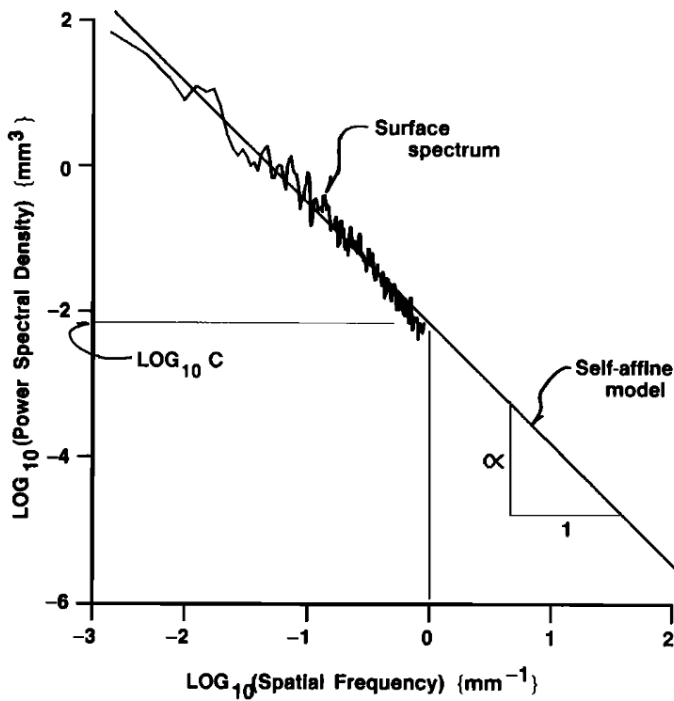


Figure 1.2. Log-log plot of a surface transect power spectral density  $P(k)$  as a function of spatial wavenumber  $k$ . A linear self-affine fractal model is fit to the surface spectrum. The model is described using two parameters  $\alpha$  (slope) and  $\log_{10}(C)$  (intercept) (From [7]).

$$P(k) \propto C k^{-\alpha} \quad (1.3)$$

The fractal scaling exponent  $\alpha$  calculated from the slope of the PSD is used to estimate the transect fractal dimension  $D$  (-), which is a measure of surface irregularity (Eq. 1.4). Additionally,  $D$  is proportional to the Hurst exponent  $H$  (-) of the surface, which is a statistical measure of autocorrelation, and is often used as an analogue for surface roughness (Eq. 1.5):

$$D = 2 - H \quad (1.4)$$

$$H = \frac{\alpha - 1}{2} \quad (1.5)$$

The Hurst exponent is advantageous as a roughness metric because it describes how roughness changes as the scale of observation changes and is thus valid across a range of measurement scales. For self-affine surfaces the Hurst exponent ranges between [0 - 1] and it has been found commonly that  $H \cong 0.8$  for granite fractures. For reference, Figure 1.3 provides a visual representation of the Hurst exponent influence on roughness along a transect. For a given 2-dimensional surface, the Hurst exponent may be measured along many 1-dimensional transects in a direction of interest and then averaged to estimate the mean  $H$ , as is performed in this thesis.

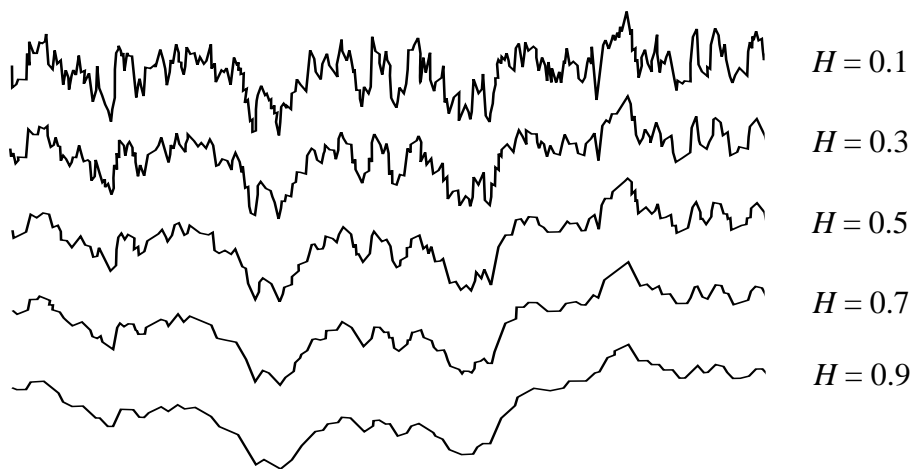


Figure 1.3. Surface profile with variable Hurst exponent  $H$ .

When considering surface roughness and its effect on flow behaviors within a fracture, it is important to also consider the spatial characterization of the fracture aperture. The aperture is classically defined as the perpendicular width between two fracture walls relative to a best fit reference plane. In contrast to surface roughness, the aperture is not an intrinsic characteristic of a fracture, though its distribution is dependent upon the position and qualities of the fracture surfaces. In this regard, the link between fracture surface morphology and the resulting aperture hydro-mechanical characteristics has been the focus of many studies [15], [16].

A related approach for examining spatial variability in datasets is the use of geostatistical metrics, including the semi-variogram. The semi-variogram (Eq. 1.6) quantifies the difference between two sampled values, termed the semi-variance, as a function of their lateral separation distance, which is termed the lag:

$$\gamma(h) = \frac{1}{2N(h)} \sum_{i=1}^{N(h)} [Z(x_i) - Z(x_i + h)]^2 \quad (1.6)$$

Where  $N(h)$  refers to the number of sampled pairs of value  $Z$  which is a function of lateral distance or lag  $h$ . The resulting graph of semi-variance  $\gamma(h)$  against lag  $h$  for a spatially distributed quantity, such as the distribution of aperture width in a fracture, typically yields a curve similar to Figure 1.4.

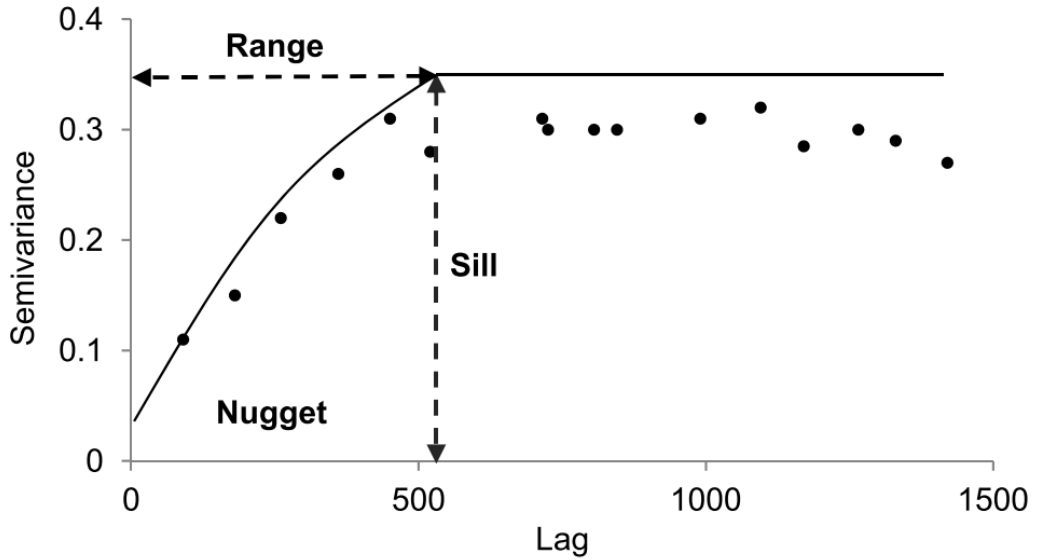


Figure 1.4. A typical semi-variogram, displaying the nugget, sill and range (From [9]).

For spatially-distributed quantities where a long-distance maximum in semivariance is achieved, the variogram is characterized by three parameters: the nugget, sill, and range, each of which provide different information about the spatial characteristics of the dataset. The nugget is the minimum value of semivariance and describes the variability between samples that are closely spaced. This effect is caused by either sampling error or inherent data variability at scales smaller than the sampling interval. The sill describes the maximum semivariance observed. As the separation distance between sampling points increases, so too does the difference in the measured values of the sampled variable. The semivariance thus

increases to a point where it reaches a limit and plateaus to a maximum value, which is the sill. The range represents the maximum distance of spatial autocorrelation and is represented on the variogram as the lag at which the sill begins – often the range is defined as the distance at which semivariance achieves 95% of the sill value. At distances smaller than the range, measured points are spatially correlated. In order to extract the nugget, sill and range from a variogram, plotted data must be fit with a theoretical model as seen in Figure 1.4 (solid line). Common models include linear, exponential, spherical, and Gaussian. For the purposes of this thesis, the spherical model will be considered, and its equation is given as:

$$\gamma(h) = C_0 + C \left[ 1.5 \left( \frac{h}{A_0} \right) - 0.5 \left( \frac{h}{A_0} \right)^3 \right] \text{ for } (h \leq A_0) \quad (1.7)$$

$$\gamma(h) = C_0 + C \quad \text{for } (h > A_0) \quad (1.8)$$

Where  $\gamma(h)$  is the semivariance measured in the unit of the spatial parameter of interest,  $h$  (m) is the lag distance,  $C_0$  is the nugget,  $C$  is the structural variance, and  $A_0$  is the range.

An advantage to the use of geostatistics over standard statistics is the ability to sample spatial dependence within a 2-dimensional dataset in any desired orientation and thus quantify the degree of anisotropy. In addition, geostatistical parameters can be estimated for disorganized or sparse datasets, whereas spectral methods such as the FFT-based fractal analysis described above requires a regular, complete grid of sampled values.

In the case of fractured media, flow behaviors are controlled most strongly by the roughness and aperture characteristics encountered parallel to the direction of flow. This observation has led to geostatistical studies of the relationship between anisotropy in fracture surface roughness and flow [9]. However, while many studies of fracture flow have used geostatistical methods to compare fracture surface roughness to flow behaviors, few have yet applied these methods to fracture aperture distributions. This approach is completed in this

thesis, with the intention of quantifying the anisotropy of the aperture width distribution and identifying the resulting effects on flow behaviors.

## 1.4. Flow in Individual Fractures: A Brief Review

The following section provides an overview of the techniques used to study flow within a single fracture. It seems appropriate to begin with the well-studied and fundamental problem of laminar flow of a viscous incompressible fluid within a parallel plate geometry. This problem has been studied by many workers including Bear 1972 [18], Louis 1969 [19] and Snow 1965 [20] who have shown that for a simplified fracture geometry consisting of two planar parallel plates, the hydraulic conductivity  $K_f$  (m/s) is given by:

$$K_f = \frac{b^2 \rho g}{12\mu} \quad (1.9)$$

As derived from the simplified Navier-Stokes equations. In this formula  $b$  (m) is the aperture between the parallel plates,  $\rho$  (kg/m<sup>3</sup>) is the fluid density,  $\mu$  (Pa · s) is the fluid dynamic viscosity, and  $g$  (m/s<sup>2</sup>) is the acceleration due to gravity. From Eq. 1.9 and Darcy's law, the volumetric flow through a fracture per unit drop in hydraulic head may be written as:

$$\frac{Q}{\Delta h} = \left( \frac{Wb}{L} \right) \left( \frac{\rho g b^2}{12\mu} \right) \quad (1.10)$$

Where  $Q$  (m<sup>3</sup>/s) is the volumetric flow rate,  $\Delta h$  (m) is the hydraulic head differential, and  $W$  (m) and  $L$  (m) are the width and length of the parallel plates respectively. Eq. 1.10 forms the basis for one of the most implemented solutions for parallel plate flow, known as the cubic law:

$$Q = W \frac{\rho g}{12\mu} b^3 \frac{\Delta h}{L} \quad (1.11)$$

While the cubic law has been shown to be valid for the case of laminar flow between planar parallel plates, flow within natural fractures often deviates from several of its assumptions [16]. For example, the aperture within a natural fracture is not geometrically constant, but rather spatially variable. Additionally, flow tortuosity has been shown to increase fluid pressure loss relative to the linear flow assumption of the cubic law. Experimental work conducted by Tsang 1984 [21] found that neglecting flow tortuosity within the parallel plate model may produce a 1-2 order of magnitude error in flow rate. Finally, the effect of contact regions or asperities within natural fractures are not considered by the cubic law. To account for these deviations from the ideal flow assumptions of the cubic law, Witherspoon 1980 [16] derived the modified cubic law:

$$Q = W \frac{\rho g}{12\mu f} b^3 \frac{\Delta h}{L} \quad (1.12)$$

In which  $f$  (-) is an empirical term. However, because  $f$  must be derived empirically for every experimental sample, the practical usage of the modified cubic law is limited. Nevertheless, due to the computational limitations of modeling flow through more realistic geometries on a large scale, the cubic law and its modified form remain widely used in fracture network models and other applications.

In the pursuit of a more realistic conceptual model for flow within irregular fractures, the local cubic law (LCL) – also known as the local Reynolds approximation – has been used. The LCL was developed from the Reynolds equation, which was formulated from the Navier-Stokes equations for use in the study of hydrodynamic lubrication of machine bearings. The Reynolds equation in its differential form describes flow between slightly nonplanar and nonparallel surfaces and is thus well-suited to approximate flow between two non-uniform fracture walls under creeping flow conditions. As derived in Milne-Thomson, 1968 [22];

Pinkus & Sternlicht, 1961 [23], in the case of steady state flow of an incompressible fluid between two irregular surfaces, the Reynolds equation can be written as:

$$\nabla \cdot \left( \frac{\rho g}{12\mu} b^3 \nabla h \right) = 0 \quad (1.13)$$

Where  $b$  (m) represents the local aperture width between the surfaces as a function of location  $(x, y)$ , and  $\nabla h$  (-) represents the local hydraulic head gradient. Several assumptions are included in the derivation of the local Reynolds equation from the Navier-Stokes equations. These include restrictions on the type of surface roughness that may be considered, with validity limited to gently sloping surfaces. Laminar flow is also assumed throughout. Additionally, it is assumed that mass and pressure continuity ( $\nabla \cdot Q = 0$ ) exists between adjacent fracture sections. Because of these governing assumptions, the LCL was thought to be an appropriate equation to describe flow within natural fractures.

The validity of the LCL in describing flow magnitudes through rough-walled fractures has been examined by many workers including Brown 1987 [24], Zimmerman 1991 [26], and Ge 1997 [28]. Results from these studies indicate that the flow predictions of the LCL deviate significantly from those of the parallel plate model if aperture variability is considered. Most notably, the LCL generally estimates less flow relative to the parallel plate model and can resolve flow channeling through high aperture regions. In laboratory experimentation, direct measurements of flow through physical fractures have been compared with the predictions of the LCL using profilometry-derived or synthetic fracture apertures [27]. Results of these studies indicate that the LCL overestimates fracture transmissivity by a factor of 40-100%, despite the use of relatively smooth fractures. It was postulated by these authors that the discrepancies were due to invalidations to the underlying assumptions of the LCL caused by either (1) inertial effects from high Reynolds numbers; (2) abrupt changes in the aperture

geometry. Additional studies showed that the LCL may be applied in limited cases where fracture surface roughness and Reynolds number are small [25]. Nevertheless, in simulating heterogeneous fracture apertures, the 2-dimensional LCL solution remains widely implemented for simulating flow in cases where approximations are sufficient due to the difficulty of implementing the 3-dimensional Navier-Stokes equations within a complex geometry.

One of the primary limitations of the 2-dimensional LCL flow solution is the assumption that the middle of the fracture aperture lies along a flat plane, whereas natural fractures exhibit a tortuous aperture plane [28]. In addition, due to aperture tortuosity and surface roughness, flow velocity profiles within realistic fractures commonly deviate from the parabolic velocity profile assumed by the LCL, in extreme cases forming flow eddies. To account for these discrepancies, modifications to the LCL have been developed by several authors [3], [28], [29]. To account for aperture plane tortuosity, Ge 1997 [28] derived a modified LCL (MLCL) which utilizes a local coordinate system to measure the aperture width perpendicular to the direction of flow ( $b_f$ ):

$$b_f(x) = b(x_i) \cos(\phi_{xi}) \quad (1.14)$$

Where  $b(x_i)$  is the apparent aperture (m) as measured normal to the x-y plane, and  $\phi_{xi}$  ( $^{\circ}$ ) is the upstream flow orientation angle. However, the verification of this MLCL was performed only for 2-dimensional parallel and non-parallel sinusoidal fractures, and therefore did not account for realistic fracture roughness. A more recent study by Wang *et al* 2015 [3] expanded upon the work of Ge 1997, formulating an MLCL which utilizes flow perpendicular aperture measurement while accounting for local roughness and inertial effects. In their formulation, an

LCL correction coefficient ( $C$ ) was calculated as a function of local aperture expansion or contraction ( $R1$ ), aperture aspect ratio ( $R2$ ), and flow Reynolds number ( $Re$ ):

$$\nabla \cdot \left[ \frac{T_x}{C(R1, R2, Re)} \frac{\partial p}{\partial x} \cos(\phi_x) \vec{i} + \frac{T_y}{C(R1, R2, Re)} \frac{\partial p}{\partial y} \cos(\phi_y) \vec{j} \right] = 0 \quad (1.15)$$

Where  $T_{x,y}$  ( $\text{m}^2/\text{s}$ ) is the transmissivity, and  $\partial p/\partial x, y$  (-) is the local pressure gradient. The MLCL in Eq. 1.15 was verified against the 3-dimensional Navier-Stokes solutions in a series of rough-walled fractures and found to estimate volumetric flow reasonably well even within tortuous fractures. Furthermore, Eq. 1.15 was found to calculate flow with lesser effective error (13.4 %) than the MLCL formulations by Ge 1997 (17.7 %), or Brush & Thompson 2003 (15.1 %) [29]. Although the MLCL in Eq. 1.15 improves upon the performance of the classical LCL, its general application is limited by several factors. Solution validity is restricted to conditions in which  $Re \leq 1$ , and the required determination of the correction coefficient  $C$  throughout the modeled domain limits its general applicability.

More complex models of flow within a single fracture have been introduced which quantify to a greater degree the internal 3-dimensional flow processes which remain unresolved in 2-dimensional approximations such as the CL, LCL or MLCL. These models are more computationally expensive and require solutions to the Stokes or Navier-Stokes equations in 3-dimensions. As a result, few studies have yet implemented these solutions successfully within irregular fracture geometries. One such study conducted by Zou et al., 2017 [6] focused upon the effect of fracture surface roughness on flow within a realistic profilometry-derived aperture geometry. Fluid flow and solute transport were simulated by directly solving the steady-state incompressible Navier-Stokes equations for flow (Eq. 1.16, Eq. 1.17):

$$\rho \mathbf{u} \cdot \nabla \mathbf{u} - \mu \nabla^2 \mathbf{u} = -\nabla P \quad (1.16)$$

$$\nabla \cdot \mathbf{u} = 0 \quad (1.17)$$

Where  $P$  (Pa) is the pressure,  $\mathbf{u}$  (m/s) is the 3-dimensional fluid velocity vector,  $\mu$  (Pa · s) is the fluid viscosity, and  $\rho$  (kg/m<sup>3</sup>) is the fluid density. This flow formulation was then and sequentially coupled to the advection-diffusion transport equation. Primary findings of the study indicated that: (1) the complex geometry of fracture surface roughness, as well as fracture contacts/closures, significantly increases the heterogeneity of flow fields within 3-dimensional rough-walled fractures, even under low  $Re$  flow conditions ( $Re = 0.001$ ). In the study, comparisons of local velocity between the 3-dimensional Navier-Stokes model and the 2-dimensional LCL flow approximation yielded -215% - 60% deviations. (2) The fracture surface roughness causes heterogeneity in the flow velocity and consequently affects transport behavior in the fracture-matrix system. Aperture heterogeneity causes dispersion of solute concentration along preferential flow channels, which becomes increasingly important at higher flow Reynolds  $Re$  and Peclet  $Pe$  numbers due to stronger advection.

Direct simulation using the Navier-Stokes and Stokes equations within 3-dimensional natural geometries currently represents the state of the art with regards to the problem of single fracture flow. Due to its difficult and computationally expensive nature, there are at present a limited number of studies that have successfully implemented this approach to solve for flow. Of this subset, there exist no studies to the author's knowledge that have yet implemented coupled solutions to solve for heat and energy exchange processes within a natural 3-dimensional fracture geometry. This is the focus of the study conducted in this thesis.

## 1.5. Heat Transfer Mechanisms in Fractured Rock:

### A Brief Review

While the previous review sections have illustrated the complexity of quantifying flow through heterogeneous fractured rock, the related problem of quantifying the resulting heat transfer capabilities of fracture-mediated flow is of great importance to researchers in various fields including radionuclide transport and geothermal systems. Prediction and evaluation of thermal production from enhanced geothermal reservoirs remains a complex problem, reliant upon a thorough understanding of convective heat transfer between fracture surfaces and the circulating fluid. Additional complexity arises when attempting to incorporate a network of fractures as is often required in field-scale geothermal reservoir models. In these systems, multiple physical processes are coupled and impacted by the fracture aperture geometry. The aperture geometry controls the distribution of primary flow channels through which fluid is transmitted. Subsequently, the distribution of high-transmissivity flow channels controls the regions of elevated heat transfer between the fracture fluid and host rock. To familiarize the reader with the nature of these coupled systems, the following provides a review of the fundamentals of heat transfer in fractures.

Heat transfer within solids, such as host rock material, occurs through conductive heat transfer, as governed by Fourier's law, which states that the rate of heat transfer through a material is proportional to the negative gradient of the material's temperature:

$$q = -k\nabla T \quad (1.19)$$

Where  $q$  is the local heat flux density ( $\text{W}/\text{m}^2$ ),  $k$  is the material's thermal conductivity ( $\text{W}/\text{m} \cdot \text{K}$ ), and  $\nabla T$  ( $\text{K}/\text{m}$ ) is the temperature gradient. In a fractured system, conductive heat transfer occurs primarily within the rock matrix, and at the fracture-fluid interface.

Heat transport in fluids is dependent upon fluid velocity within the fracture, and is governed by the heat advection-diffusion equation:

$$\rho C_p \frac{\partial T}{\partial t} + \rho C_p \mathbf{u} \cdot \nabla T + \nabla \cdot q = Q \quad (1.20)$$

Where  $\rho$  ( $\text{kg}/\text{m}^3$ ) is the fluid density,  $C_p$  ( $\text{J}/\text{kg} \cdot \text{K}$ ) is the specific heat capacity of the fluid,  $\mathbf{u}$  ( $\text{m}/\text{s}$ ) is the fluid velocity field,  $\nabla T$  ( $\text{K}/\text{m}$ ) is the temperature gradient,  $q$  ( $\text{W}/\text{m}^2$ ) is the conductive heat flux entering the fluid from Eq. 1.19, and  $Q$  ( $\text{W}$ ) contains any internal sources or sinks of heat within the system. In a fractured system, advection of heat occurs as heated fluid migrates through the aperture, thereby transporting energy with its motion.

One aspect critical to conductive heat transfer in fractures is the development of boundary layers at solid-fluid interfaces. In fracture systems characterized by laminar flow, viscous boundary layers develop as thin layers at the fracture wall where the fluid velocity approaches zero. Within viscous boundary layers, fluid velocities are sufficiently slow to assume conductive heat transfer dominates throughout these fluid areas as well. Importantly, viscous boundary layer thickness is dependent upon several factors including local fluid velocity and fracture surface roughness.

An important consideration when examining heat transfer efficiency within a system is the relative dominance of the mechanisms involved. One metric utilized to determine the relative strength of advection and conduction within a fluid is the dimensionless Peclet number. The Peclet number can be calculated for any conservative quantity including heat and is the ratio of advective to diffusive transport:

$$Pe = \frac{\text{advective transport rate}}{\text{diffusive transport rate}} = \frac{U * L}{\alpha} \quad (1.21)$$

Where  $U$  (m/s) is the fluid velocity magnitude,  $L$  (m) is the characteristic length considered, and  $\alpha$  (m<sup>2</sup>/s) is the thermal diffusivity of the fluid. In addition to its utility as a metric for relative advective strength, the dimensionless nature of the Peclet number makes it useful in dimensional analysis and model upscaling. This function of the Peclet number is utilized later in the work of this thesis.

## 1.6. Solutions to Heat Transport in Fractured Rock:

### A Brief Review

Modeling of heat transfer in fractured systems is often a data-limited exercise. Commonly, the actual geometry of the system cannot be determined, and thus a simplified geometric representation is required for analytical approaches. In discrete fracture models, the geometry of each individual fracture is considered, but typically approximated as a pair of parallel and planar fracture walls. It therefore seems prudent to supplement this review with an analysis of the analytical and numerical approaches applied to the problem of parallel plate flow and heat exchange. This fundamental problem has been studied for decades by workers in fluid mechanics and heat transfer due to the numerous industrial, chemical, and engineering applications [30], [31], [32], [33], [34]. As a result, many coupled analytical and numerical solutions exist in the literature ranging in scale from the discrete fracture to the aquifer. This section will focus upon both analytical and numerical solutions developed for applications related to geothermal energy production.

The case we will consider first is the two-dimensional semi-analytical steady-state solution to the heat transport problem within a series of discrete fractures as developed by Bodvarsson & Tsang 1982 [31]. This solution was developed for the problem of an injection well penetrating a series of infinite, parallel, equidistant horizontal fractures separated by blocks of homogeneous impermeable rock. The considered geometry is shown in Figure 1.5.

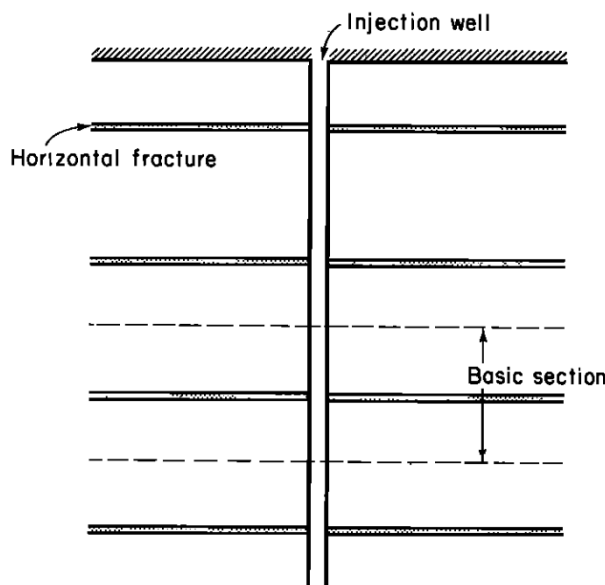


Figure 1.5. Cross-section of the analytical model developed by Bödvarsson and Tsang 1982, [31].

This solution makes use of the geometrical symmetry about the dashed lines in Figure 1.5, thus a single basic section of the fracture system may be analyzed, as shown in Figure 1.6.

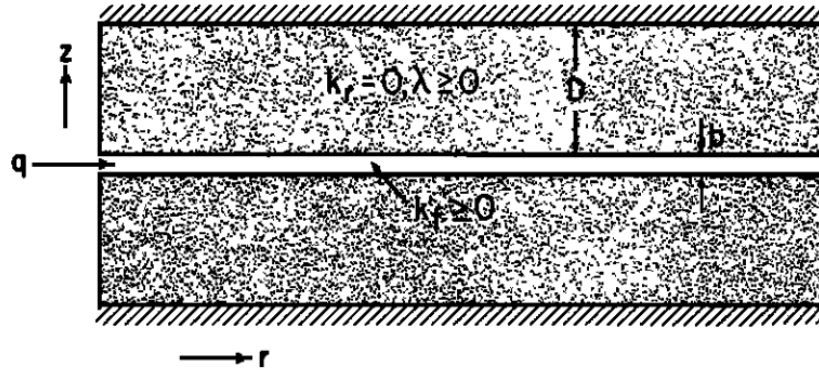


Figure 1.6. A basic section of the fracture system considered in Figure 1.5 (From [31]).

Several assumptions are included in the model. Flow within the fracture is assumed to be steady and purely radial, with the well located at  $r = 0$ . In the fracture aperture, temperature and flow velocity are assumed to vary only as a function of radius, and the temperature of the fluid is equal to the rock matrix temperature. The solution method implemented in the study is dependent upon the use of dimensionless parameter substitutions, which are used to form a coherent set of dimensionless governing equations. Via this method, this model can calculate the temperature profile within the fluid and rock at any time, in addition it can calculate transient movement of the thermal front. An advantage to the semi-analytical approach derived by Bödvarsson and Tsang is the rapid and exact calculation of temperature, which provides a reliable solution against which numerical solutions can be verified. However, the realism of this solution is impaired due to the greatly simplified geometry of the fracture network, which may not capture the complexity of a natural aquifer. Several characteristics important to flow and transport are neglected including aperture variability, flow tortuosity, and longitudinal diffusion of heat.

Except in some simple and idealized cases, the partial differential equations and boundary conditions required to model flow and transport within fractures cannot be solved analytically. In order to accurately model the complexities inherent to natural geothermal systems, numerical approaches are often used. While numerical modeling techniques are computationally expensive relative to analytical approaches, advances in modern computational technology have greatly enhanced their feasibility. The flexibility of numerical methods has made them popular for modeling a host of physical processes including flow and heat transfer from the fracture to reservoir scale.

Numerical models used in reservoir scale studies commonly employ a discrete fracture scheme in which the physical processes of each individual fracture are accounted for. Discrete fracture network (DFN) models commonly represent conducting fractures as discrete planar features within a realistic three-dimensional reservoir system. While this modeling approach is effective in capturing the variable connectivity of natural fracture networks, geometric simplifications are still relied upon for individual fractures. In this context, stochastic algorithms such as GEOFRAC® or FRACMAN® are often used to generate realistic fracture networks [2].

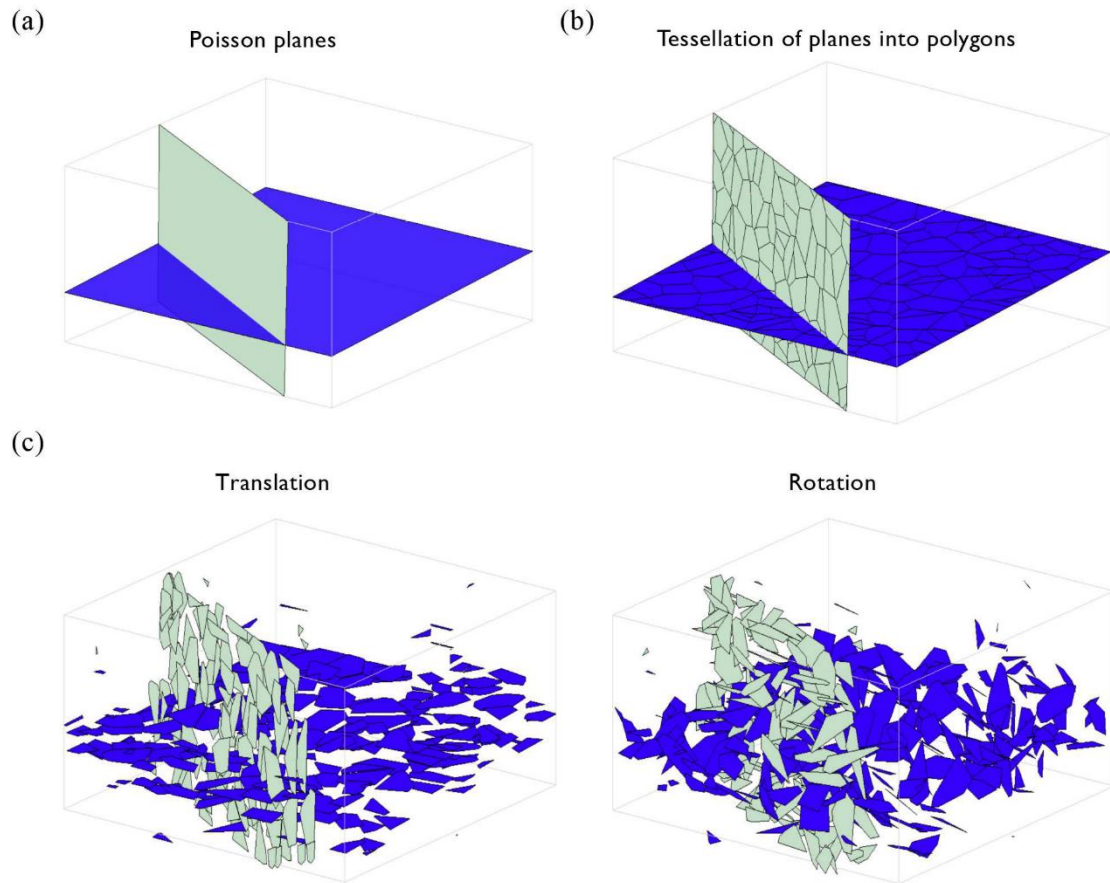


Figure 1.7. Stochastic discrete fracture network generation using the GEOFRAC® model. (From [2]) (a) Primary stochastic process: Poisson plane generation. (b) Secondary stochastic process: Poisson-Voronoi tessellation of planes. (c) Tertiary stochastic process: random translation and rotation of polygons.

Figure 1.7 illustrates the stochastic fracture network generation process used by GEOFRAC®. Within a DFN geometry, coupling of flow and heat transfer processes along the primary flow path is simplified to a one-dimensional heat exchange problem for flow between parallel plates. While stochastic realizations of fracture networks used in DFN models may capture greater geometric connectivity relative to the parallel fracture solution implemented by Bödvarsson and Tsang 1982, the assumption of parallel plate flow and heat transfer idealizes the underlying physical processes. To address this, more sophisticated models are required which include the effects of aperture variability and flow tortuosity on flow and heat transfer within a discrete fracture geometry.

## 1.7. Point of the Current Contribution

Although its inability to fully characterize flow behaviors within rough-walled geometries has been thoroughly demonstrated [21], [24], the ubiquity of the parallel plate approximation for describing fracture flow and heat exchange persists in many applications. In reality, fracture surface variability and aperture heterogeneity produce velocity variance and channelization behaviors which are otherwise unaccounted for in simplified geometric approximations. Deviations in flow behaviors from the cubic law almost certainly have significant effects on heat exchange characteristics within fractures, but studies in this regard are lacking.

To account for this, the primary goal of this thesis was to investigate the effect of fracture surface roughness on flow and energy exchange processes within a realistic three-dimensional fracture geometry. Another focus of this work was upon the use of geostatistical methods to characterize aperture heterogeneity. The purpose of this was to establish observable relationships between spatial aperture characteristics, and flow and energy exchange behaviors.

To accomplish these goals, several numerical models for fracture flow were developed from realistic fracture surfaces. Fracture surface realism was attained through: (1) laboratory triaxial fracturing of granite samples, (2) white-light interferometry acquisition of granite fracture surfaces for use in modeling. Creation and geostatistical measurement of model apertures was performed in MATLAB<sup>®</sup>, and three-dimensional coupled flow and heat transfer modeling was performed in COMSOL Multiphysics<sup>®</sup>. Lastly, numerical model outputs were validated against an established analytical solution.

The remainder of this thesis discusses the research in detail and is organized as follows: Chapter 2 summarizes the creation, acquisition and spatial analysis of the natural granite fracture geometries used in numerical modeling. Chapter 3 discusses the numerical model configuration and scheme within COMSOL Multiphysics®. Chapter 4 shows the results from modeling, discusses the main experimental findings, and comments upon agreement with analytical solution. Chapter 5 summarizes the main conclusions of this work and provides suggestions for future studies.

## 2. Development & Characterization of Natural Rock Fractures

Of primary interest in this work was the simulation of flow processes within a realistic and well characterized fracture geometry. To accomplish this, the digital acquisition of natural granite fracture surfaces was required for use as a numerical model input. An additional benefit of this process was the ability to perform thorough statistical analyses on the digitized surfaces and resulting apertures, which can be used to then generate realistic synthetic fractures. This chapter describes the process followed in the acquisition, composition, and analysis of the natural granite fractures used in later numerical modeling.

### 2.1. Sample Selection and Preparation

Sierra granite was selected as a suitable material for fracturing due primarily to its near isotropic compressional failure behavior. Five core samples of 1.5-inch diameter and 3.5-inch length were cored from a block of Sierra granite using a Jet J-720R radial arm drill press. Core samples were notched via water jet twice each at  $60^{\circ}$  angles to the long dimension of the sample to initiate planar fracture formation. Core samples were then prepared for triaxial testing via precision saw removal of irregular end caps.

The five granite core samples (SG-001 – SG-005) were prepared for fracturing via triaxial compression. Samples were each jacketed with 1.5 mm thick heat-shrink wrap and sealed via heat application. Sample notches were filled with granular silica particles prior to jacketing to avoid premature tearing from radial loading during confining pressure application. A GCTS® RTR-1000 triaxial testing apparatus was utilized to apply variable confining

pressures and axial load. During triaxial testing, confining pressure was first applied and axial load was subsequently increased until compressional failure was achieved (Table 2.1). Following compressional failure, samples were inspected for confining oil intrusion indicative of jacket failure during confining pressure loading. Samples with an absence of internal confining oil were selected for surface acquisition (SG-001 - SG-003, SG-005).

## 2.2. Natural Fracture Surface Acquisition

### 2.2.1. *White-light Interferometry*

Fractured samples were carefully separated along a single dominant fracture plane such that any fault gouge was reasonably preserved in its original location. Three-dimensional fracture surface data was then acquired using a Nanovea® JR-25 non-contact white-light interferometer (WLI) at 10  $\mu\text{m}$  horizontal and 0.1  $\mu\text{m}$  vertical spatial resolution. Suitably mated 3.00 x 4.00-centimeter surfaces of the hanging and footwall portions of each sample fracture were scanned, with the longer dimension (henceforth, X-dimension) parallel to the direction of shear. Two scans of each fracture surface were acquired, the first with fault gouge present, and the second once fault gouge was removed via thorough surface brushing. It was determined during post-processing that the scans acquired with fault gouge present could not be used for further modeling due to the presence of surface artifacts caused by diffuse scattering of the WLI beam. The surface acquisition process was repeated for each of the Sierra granite samples which were unaffected by confining oil intrusion (SG-001 - SG-003, SG-005) for a total of 16 scans (i.e., each of 2 surfaces from 4 fractured rock samples, with and without gouge).

## 2.3. Natural Aperture Composition

Granite surface scans acquired via WLI were processed using MountainsMap® 7.4 to remove spatial outliers as a result of anomalously strong or weak surface reflections. Surfaces were loaded individually and not-measured (NM) points were filled via a nearest-neighbor mean value interpolation function within MountainsMap®. Outliers were removed via the MountainsMap® outlier removal algorithm which identifies problematic points based upon high signal-to-noise ratio and local slope variations. Outlier interpolation was required for 0 - ~5% of fracture surface area with varied extent between samples. Following outlier removal, NM points were again filled in via an internal nearest-neighbor mean value interpolation function. Following processing and outlier removal, several surfaces were deemed unusable for further experimentation due to either to highly irregular fracture planes (SG-001), poor surface acquisition due to triaxial oil submersion (SG-004), or prominent scan artifacts which were resistant to denoising operations (SG-005). Suitable surfaces from samples SG-002 and SG-003 were exported to MATLAB for fracture aperture composition and further analysis.

Once imported to MATLAB, fracture surfaces were utilized to produce fracture apertures with natural roughness. To remove slope artifacts from the scanning process, loaded surfaces were two dimensionally leveled via small angle rotations relative to the X and Y surface axis. Aperture generation was accomplished via duplication of a surface scan and separation by 0.5 mm normal to the plane of the surface similar to the technique used in Zou 2017 [6]. This technique was used to produce a constant and homogeneous aperture distribution. In other cases, surfaces were laterally displaced following aperture separation to introduce aperture heterogeneity. Asperities—points of surface intersection produced by shearing—were replaced with a minimal aperture width of 0.2 mm to avoid self-intersecting

faces for modeling purposes. Following separation and possible displacement, the coordinates of the upper and lower surfaces corresponding to 3.00 cm x 3.00 cm (3,000 x 3,000-pixel) sections of interest were written to a stereolithography file (.stl) at 10- $\mu\text{m}$  horizontal spatial resolution for further processing. In total, two natural aperture geometries ( $H = 0.93_{\text{HOM}}$ ,  $H = 0.93_{\text{HET}}$ ) were created from the same granite surface scan (SG-002 Lower) corresponding to lateral displacement magnitudes of 0, and 1.5 mm (Table 2.5). Figure 2.1-A depicts the natural aperture field produced as a result of 1.5 mm of shear displacement of the SG-002 Lower surface.

## 2.4. Fracture Spatial Statistics

### 2.4.1. Fracture Surface Roughness Analysis

Hurst exponent  $H$  and root mean square height  $Rq$  were measured on fracture surfaces in the X and Y-parallel directions to assess the effect of roughness anisotropy on flow and heat transfer processes. In order to acquire a valid estimate of  $Rq$ , the measured surface was first two-dimensionally detrended via removal of the best planar fit in MATLAB.  $Rq$  was measured for a discretized and detrended surface transect of interest via Eq. 2.1:

$$Rq = \sqrt{\frac{1}{N} \sum_{i=1}^N z_i^2} \quad (2.1)$$

Where  $N$  denotes the number of discretized measurement points along the transect, and  $z$  represents the surface height deviation from the mean height of the measured length. Directionally averaged  $Rq$  for acquired granite fracture surface height was calculated on  $N = 3,000$ -pixel transects.  $Rq$  was calculated for 3,000 transects for each fracture surface and

averaged to determine the arithmetic mean roughness  $Rq_m$  in each direction. Results from these calculations are presented in (Table 2.3) for surfaces from granite samples SG-002, SG-003.

Similarly, mean Hurst exponents for all fracture surfaces are estimated in both X and Y-parallel directions via 1-dimensional transect Hurst exponent calculation and averaging. The Hurst exponent is estimated via two methods for measurement fidelity.

The first method is a spectral approach, which examines spatial variability over a range of surface wavelengths. In this method, a surface's power spectral density (PSD) is computed from transect topography data. The longest and shortest wavelengths which can be accurately used correspond to the transect length, and the length corresponding to double the sampling interval, in this study 0.03 m and 20  $\mu\text{m}$  respectively. The one-sided amplitude spectrum for each transect is squared and normalized by the spatial wavenumber to calculate the transect PSD. A power law (Eq. 2.2) is fit to each transect, and the Hurst exponent is obtained from evaluation of the power law slope  $\alpha$  (Eq. 2.3). Via this method, the Hurst exponent is estimated for each surface transect and averaged over all transects to obtain a mean surface Hurst exponent.

$$P(k) = Ck^{-\alpha} \quad (2.2)$$

$$H = \frac{\alpha - 1}{2} \quad (2.3)$$

The second method of surface Hurst exponent estimation involves evaluation of the generalized Hurst exponent via rescaled range (R/S) analysis. The rescaled range for a given surface transect is calculated as follows. First, the 3000-pixel transect is broken into the following: two transects of 1,500-pixel length, four transects of 750-pixel length, and eight transects of 375-pixel length. For each segment, the following operations are performed. The mean height of the transect is calculated and subtracted from the transect to produce a mean-

adjusted transect topography. The standard deviation  $\sigma$  of the mean centered values is calculated. The cumulative deviate series is calculated via summation of deviations from the mean. The range  $R$  is calculated by subtracting the maximum from the minimum value of the cumulative deviate series. For each segment, the rescaled range is calculated by dividing the range  $R$  by the standard deviation  $\sigma$ . Once plotted, the rescaled range and the segment length follow a power law for natural fracture surfaces (Eq. 2.4), where the Hurst exponent describes the slope of the relation. Similarly, to the spectral method, the generalized Hurst exponent is evaluated for surface transects individually in the flow-parallel and flow-perpendicular directions and averaged to determine the directional Hurst exponent.

$$R(L) = CL^{-H} \quad (2.4)$$

Directional Hurst exponent measurements obtained from both the PSD and R/S methods upon the surfaces from granite samples SG-002, SG-003 are presented in (Table 2.3). To ensure measurement fidelity, the PSD and R/S methods were each implemented upon synthetic calibration surfaces of constrained Hurst exponent ( $H = 0.75, 0.90$ ). The precision of each method was quantified via RMSE calculation of error from the constrained surface  $H$  value. While both methods estimated  $H$  with reasonable precision, calculated RMSE was lower when the R/S method was used, and thus measurements referenced throughout this thesis report the R/S estimated Hurst exponents.

Directional estimation of surface Hurst exponent from the SG-002 and SG-003 granite fractures yielded several interesting trends in roughness anisotropy. It can be observed from (Table 2.3) that  $H$  estimates vary with measurement direction. Universally, X-direction (slip-parallel)  $H$  estimates reflect rougher topography relative to Y-direction (slip-perpendicular) estimates. In addition, the magnitude of roughness anisotropy tends to correlate with the

confining pressure under which the fracture was initiated, with greater roughness anisotropy characteristic of higher confining pressures. It is also generally observed that fracture surfaces possess lower  $H$  (greater roughness) when initiated under greater confining pressures. These findings are consistent with recent studies conducted upon the confining pressure dependence of fracture roughness in granite [35].

Measured natural surface  $H$  and RMS roughness ( $R_q$ ) values were used as reference to create synthetic fracture surfaces of realistic but varied roughness. One objective of this was to explore the effects of surface roughness on flow and energy exchange over a wide range of roughness values typical in geologic media, but not represented within the acquired granite fractures. A second objective was to observe how effectively a synthetically generated surface can emulate the properties of realistic fracture geometry. Thus, synthetic surfaces possessing characteristics consistent with extremely rough media ( $H = 0.75$ ,  $R_q = 1.1$  mm) and fractured granite ( $H = 0.90$ ,  $R_q = 1.1$  mm) were generated for flow and heat transfer experimentation (Table 2.4). These surfaces were used to create synthetic apertures with a method similar to that described in Section 2.3 (Figure 2.1). This process is explored in detail in Chapter 3.

#### *2.4.2. Statistical Fracture Aperture Analysis*

A finite amount of slip can be expected to produce aperture variability with a distinct maximum. For this reason, trends in the spatial distribution and correlation of the aperture width field were assessed via geostatistical methods. Directional variability in aperture width correlation length was assessed via calculation of the anisotropic variogram. Six variograms were calculated in 30-degree sampling orientations for each aperture and fit with a spherical model to calculate the resulting range, sill, and nugget. Composite variogram range values

were calculated in each orientation via averaging of the three most closely oriented variogram range outputs (Figure 2.1-B). Additionally, the variance and mean aperture width is recorded for each shear-displaced heterogeneous aperture for use in comparison with parallel-plate models, as discussed further in Chapter 3.

Figure 2.1 provides a visual comparison of the relationship between aperture width distribution and measured geostatistical parameters. Figure 2.1-B,D,F shows the calculated variogram range (correlation length) for the natural ( $H \approx 0.93_{HET}$ ) and synthetically generated ( $H \approx 0.90_{HET}, H \approx 0.75_{HET}$ ) shear-displaced fracture apertures. It should be noted that the X axis is parallel to the direction of shear. It can be observed that correlation lengths for two out of three of the apertures are longest in the shear perpendicular direction. This is thought to be caused by the opening of elongate channels due to surface shear, and is reflected in the aperture width distributions (Figure 2.1-A,C,E). A notable deviation from this is the  $H = 0.90_{HET}$  model, which exhibits the longest correlation close to the shear-parallel direction. It is speculated that this is due to the presence of asperities near the central reference point used in measurements of the anisotropic variogram. Asperities exhibit a constant aperture width and thus their presence may cause overestimation of correlation length measurements. In addition to these observations, it can be noted that mean correlation length decreases with increasing surface roughness. This relationship is further explored in Chapter 4 and shown to have implications for flow and heat transfer behaviors within heterogeneous apertures.

## 2.5. Tables

Table 2.1: Triaxial testing results

Sample	Confining Pressure [MPa]	Axial Failure [MPa]	Result
SG-001	10	233.13	Unusable surface
SG-002	20	291.12	Successful
SG-003	5	205.68	Successful
SG-004	20	298.48	Oil leak; Unusable
SG-005	10	246.12	Unusable surface

Table 2.2: Scan acquisition parameters

Parameter	Unit	Value(s) used in this study
Spatial resolution (X-Y)	µm	10.0
Spatial resolution (Z)	µm	1.0
Scan dimensions (X-Y)	mm	40.0 x 30.0

Table 2.3. Measured Fracture Surface Hurst exponent ( $H$ ) From R/S and PSD Methods. Measured RMS roughness also reported for reference. Method RMSE from  $H$  measurements on synthetic calibration surfaces of constrained  $H$  presented.

Surface	Measurement direction	Hurst exponent (R/S method) [-]	Hurst exponent (PSD method) [-]	RMS roughness [mm]
SG-002 Lower	X, Y	0.921, 0.952	0.932, 0.949	1.140, 1.173
SG-002 Upper	X, Y	0.932, 0.955	0.954, 0.987	1.137, 1.163
SG-003 Lower	X, Y	0.839, 0.879	0.864, 0.894	0.991, 1.016
SG-003 Upper	X, Y	0.834, 0.871	0.851, 0.887	1.115, 1.069
$H = 0.75$ calibration (RMSE)	X, Y	0.764, 0.762 (0.013)	0.784, 0.787 (0.035)	
$H = 0.90$ calibration (RMSE)	X, Y	0.894, 0.890 (0.008)	0.929, 0.927 (0.028)	

Table 2.4. Parameters used to generate synthetic fracture apertures

Parameter	Unit	Value(s) used in this study
Surface Hurst exponent ( $H$ )	-	0.750, 0.900
Surface RMS roughness ( $Rq$ )	mm	1.1
Aperture separation	mm	0.5
Surface shear (X-direction)	mm	0, 1.5

Table 2.5 Apertures created with natural granite WLI surfaces with standard statistics denoted. Subscript  $HOM$  refers to homogeneous aperture due to no fracture surface shear, subscript  $HET$  refers to heterogeneous apertures produced by X-direction surface shear.

Aperture Model	Surface Used	Surface Shear [mm]	Mean Aperture Width [mm]	Aperture Variance [mm <sup>2</sup> ]	Asperity Area [%]
$H = 0.93_{HOM}$	SG-002 Lower	0	0.500	0	0
$H = 0.93_{HET}$	SG-002 Lower	1.5	0.707	0.065	5.094

## 2.6. Figures

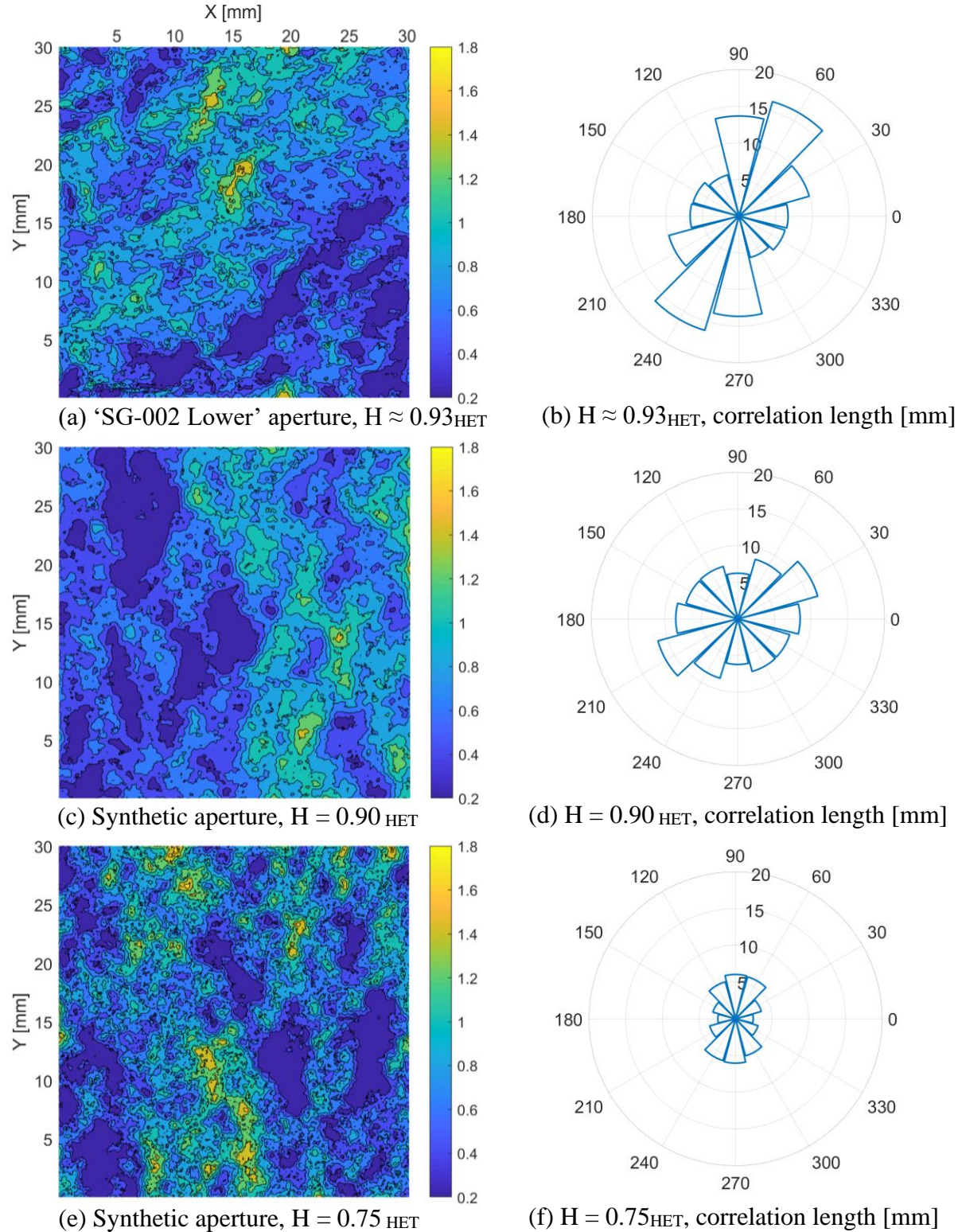


Figure 2.1. Analysis of aperture fields generated using natural ( $H = 0.93_{\text{HET}}$ ), and synthetic ( $H = 0.90_{\text{HET}}$ ,  $H = 0.75_{\text{HET}}$ ) surfaces subject to 1.5 mm of relative shearing in the X-direction.

### 3. Simulation of Flow & Heat Exchange in Natural & Synthetic Rock Fractures

#### 3.1. Modeling Software

COMSOL Multiphysics® is a finite element analysis, solver and simulation software package for various physics and engineering applications. The software was chosen for this work because of its availability, and its modular structure. The modular structure of COMSOL® allows the user to easily add or subtract different “physics” packages – such as fluid flow in different regimes and heat transfer – and couple them intuitively. COMSOL® can also connect physics used within different domains - for example, allowing the study of heat advection and transport within a flowing fluid while connecting this to surrounding domains of rock in which heat diffusion is modeled. COMSOL® inherently links energy or mass fluxes across boundaries between different problem domains, i.e., ensuring balances of heat fluxes across domains. Furthermore, COMSOL® allows the user to create studies that are stationary (steady state) and/or transient which is ideal in the case of coupling fluid flow and heat transfer. The remainder of this chapter discusses the creation of synthetic and natural fracture models in COMSOL® and results found from the numerical simulations.

### 3.2. Synthetic Fracture Surface & Aperture Composition

In addition to the natural fracture surfaces discussed in Chapter 2, several synthetic surfaces were generated with similar geometric parameters to fractured sierra granite for model output comparison. 6.00 cm x 6.00 cm isotropically rough synthetic surfaces were created in MATLAB as 6,000 x 6,000-pixel matrices from input spatial resolution, root-mean-square (RMS) roughness, and radially averaged Hurst exponent ( $H$ ) values (Table 2.4).

To generate each aperture, a single synthetic surface was duplicated and separated by 0.5 mm normal to the plane of the surface. If required, surfaces were laterally displaced in the X-direction following the aperture separation step. Due to difficulties encountered when meshing self-intersecting faces, asperities produced during lateral shear displacement were replaced with a minimum aperture separation of 0.2 mm. This was accomplished via individual replacement of intersecting pixels on each surface with half of the aperture intersection magnitude to create a flush face. Following pixel replacement, the upper and lower surfaces were rigidly separated by 0.2 mm to create a uniform minimal aperture. Following aperture composition, the coordinates of the upper and lower surfaces corresponding to 3.00 cm x 3.00 cm (3,000 x 3,000-pixel) sections of interest were written to a standard tessellation language file (STL) at 10  $\mu\text{m}$  spatial resolution for further processing. In total, four synthetic apertures ( $H = 0.75_{\text{HOM}}$ ,  $H = 0.75_{\text{HET}}$ ,  $H = 0.90_{\text{HOM}}$ ,  $H = 0.90_{\text{HET}}$ ) were created corresponding to combinations of Hurst exponent ( $H = 0.75, 0.9$ ) and lateral displacement: 0 mm; homogeneous aperture, 1.5 mm; heterogeneous aperture (Table 3.2). Figure 2.1-C and E depicts the synthetic aperture fields produced as a result of 1.5 mm of X-direction shear displacement.

### 3.2.1. *MeshLab® and Netfabb® Aperture Geometry Pre-Processing*

Due to the computational limits of the COMSOL® STL-to-CAD algorithm, coarsening of each aperture geometry mesh is required prior to import. Each mesh is adaptively coarsened by a factor of 0.025 corresponding to a 97.5% reduction in the number of faces from  $3.6 * 10^7$  to  $9.0 * 10^5$ . Mesh coarsening is applied utilizing the MeshLab® quadric edge collapse decimation (QECD) simplification algorithm. The simplification algorithm is calibrated to ensure preservation of surface normals, and topology during face reduction. Use of the planar simplification script ensures the most significant compression occurs along the planar wall boundaries of each aperture geometry rather than the fracture face. Additionally, a mesh element quality threshold of 1.0 was selected to reduce the number of poor-quality triangular faces. Following QECD simplification, aperture meshes are imported to AutoDesk NetFabb® for additional repair operations. Self-intersecting, duplicate, normal-flipped, and zero area faces are identified and removed via the internal extended mesh repair algorithm. Internal holes formed from the removal of erroneous faces are then filled via an additional MeshLab® filter process. Following preprocessing, the STL aperture meshes are ready for COMSOL® import as model geometry components.

### 3.3. Model Geometry

The sizes of the COMSOL® models created are limited primarily by a need to maintain high spatial resolution within regions of interest while not exceeding computational capacity available. The greatest emphasis is placed upon achieving high spatial resolution of the fracture surfaces, which limits their lateral extent to 3.00 cm x 3.00 cm. All models were composed of two domains. Domain one is the fracture aperture volume (3.00 x cm 3.00 cm x  $W_m$ ) (where  $W_m$  is the mean aperture width, typically ~0.7 mm) which varies in vertical extent due to minor slope and surface displacement effects. The domain is set as water from COMSOL's® built-in materials. Domain two extends above and below the fracture aperture volume (3.05 cm x 3.05 cm x 6.00 cm +  $W_m$ ) and encompasses domain one on all sides. Domain two is set as granite from COMSOL's® built-in materials.

## 3.4. Physics and Boundary Conditions

### 3.4.1. Physics

In the models, the heat transfer and laminar flow modules are utilized and coupled by the non-isothermal flow multiphysics module. The conjugate heat transfer module was applied to both model domains. The conjugate heat transfer module uses the heat diffusion equation for solids and the heat advection-diffusion equation for fluids to solve for temperature everywhere in the model. Thermal flux continuity on the fracture interface is ensured with an identity pair coupling. The physics for steady-state heat transfer in a solid are represented by the following equations:

$$\rho C_p \mathbf{u} \cdot \nabla T + \nabla \cdot \mathbf{q}_T = Q + Q_{ted} \quad (3.1)$$

$$\mathbf{q}_T = -k \nabla T \quad (3.2)$$

Where  $\rho$  is the density of the solid,  $C_p$  is the heat capacity of the solid at constant pressure,  $\mathbf{u}$  is the translational motion vector, which is equal to zero in the solid domain,  $\nabla T$  is the temperature gradient across the solid,  $Q$  contains additional heat sources,  $Q_{ted}$  is heat from thermoelastic damping,  $k$  is the thermal conductivity of the solid, and  $\mathbf{q}_T$  is the conductive heat flux.

In fluid portions of the model domain, heat advection is solved by coupling to a Navier-Stokes solver for the fluid velocity. Equations are shown below:

$$\rho C_p \mathbf{u} \cdot \nabla T + \nabla \cdot \mathbf{q}_T = Q + Q_p + Q_{vd} \quad (3.3)$$

$$\mathbf{q}_T = -k \nabla T \quad (3.4)$$

Where  $\rho$  is the temperature-dependent density of the fluid,  $C_p$  is the heat capacity of the solid at constant pressure,  $\mathbf{u}$  is the translational motion vector solved with the Navier-Stokes continuity equations,  $\nabla T$  is the temperature gradient across the solid,  $Q$  contains additional heat

sources,  $Q_{ted}$  is heat from thermoelastic damping,  $Q_{vd}$  is heat from viscous dissipation of the fluid,  $k$  is the thermal conductivity of the fluid, and  $\mathbf{q}_T$  is the conductive heat flux.

The laminar flow module is applied to only the fracture aperture domain. The laminar flow module uses the Navier-Stokes continuity equations to solve for fluid velocity everywhere within the aperture domain. The fluid is assumed to be incompressible, with gravity, turbulence, and inertial effects assumed to be negligible. Equations are shown below:

$$\nabla \cdot [-p\mathbf{I} + \mu(\nabla\mathbf{u} + (\nabla\mathbf{u})^T)] + \mathbf{F} = 0 \quad (3.5)$$

$$\rho\nabla \cdot \mathbf{u} = 0 \quad (3.6)$$

Where  $p$  is pressure,  $\mu$  is the temperature-dependent dynamic viscosity,  $\rho$  is the temperature-dependent density of the fluid,  $\mathbf{I}$  is the identity matrix,  $\mathbf{n}$  is the boundary normal pointing out of the domain,  $\mathbf{F}$  is the vector of external forces applied to the fluid, and Eq. 3.6 is the continuity equation.

### 3.4.2. Boundary and Initial Conditions

Boundary and initial conditions are required in COMSOL® for fluid velocities  $\mathbf{u}$  and temperature  $T$ . The temperature boundary conditions are represented as follows: the distal upper and lower granite boundaries shown in Figure 3.2-E are specified temperature boundary conditions. These boundary conditions are represented by the equation shown below:

$$T = T_0 \quad (3.7)$$

Where  $T$  is the temperature and  $T_0$  is the boundary temperature set by the user. See Table 3.1 for selected boundary condition model parameters. The fracture inlet and outlet, shown in Figure 3.2-A, B, are thermal inflow and outflow boundary conditions respectively. These allow heat flux from the interior of the fracture to the exterior of the model at a rate proportional to

the fluid velocity and boundary temperature gradient. These boundary conditions are represented by the equation shown below:

$$-\mathbf{n} \cdot \mathbf{q}_T = p\Delta H \mathbf{u} \cdot \mathbf{n} \quad (3.8)$$

Where  $\mathbf{n}$  is the boundary normal,  $\mathbf{q}_T$  is the heat flux,  $\mathbf{u}$  is the fluid velocity, and the thermal gradient  $\Delta H$  is calculated from the upstream temperature and pressure  $p$ :

$$\Delta H = \int_{T_{upstream}}^T C_p dT + \int_{p_{upstream}}^p \frac{1}{p} (1 - \alpha_p T) dp \quad (3.9)$$

Where  $\alpha_p$  is the thermal diffusivity of water. Thermal insulation boundaries are applied to the sides of the fracture, and to the external granite domain surfaces as shown in Figure 3.2 D, F. No heat flux can occur across these boundaries, and the condition is represented by the equation shown below:

$$-\mathbf{n} \cdot \mathbf{q}_T = 0 \quad (3.10)$$

Where  $\mathbf{n}$  is the boundary normal pointing out of the domain, and  $\mathbf{q}_T$  is the heat flux.

Laminar flow boundary conditions are represented as follows: the fracture inlet shown in Figure 3.2-A is a laminar inflow boundary condition represented by the equation shown below:

$$L_{entr} \nabla \cdot [-p\mathbf{I} + \mu(\nabla\mathbf{u} + (\nabla\mathbf{u})^T)] = -p_0 \mathbf{n} \quad (3.11)$$

Where  $p_0$  is inlet pressure,  $\mathbf{I}$  is the identity matrix,  $\mathbf{n}$  is the boundary normal pointing out of the domain,  $\mu$  is the temperature-dependent fluid dynamic viscosity, and  $L_{entr}$  is the hydrodynamic entrance length which is equal to zero for fully developed flow. The fracture outlet shown in Figure 3.2-B is a constant pressure boundary condition and is represented by the equation shown below:

$$[-p\mathbf{I} + \mu(\nabla\mathbf{u} + (\nabla\mathbf{u})^T)]\mathbf{n} = -\hat{p}_0 \mathbf{n} \quad (3.12)$$

Where  $\hat{p}_0$  is the outlet pressure equal to 0 kPa,  $\mathbf{I}$  is the identity matrix,  $\mathbf{n}$  is the boundary normal pointing out of the domain,  $\mu$  is the temperature-dependent fluid dynamic viscosity, and  $\mathbf{u}$  is the fluid velocity. The fracture surfaces shown in Figure 3.2-C are no slip boundary conditions represented by the following equation:

$$\mathbf{u} = 0 \quad (3.13)$$

Where  $\mathbf{u}$  is the fluid velocity vector at the fracture interface. The sides of the fracture aperture are slip boundaries used to reduce velocity artifacts from the laterally enclosed domain. These boundaries are represented by the following equations:

$$\boldsymbol{\kappa} = [\mu(\nabla\mathbf{u} + (\nabla\mathbf{u})^T)]\mathbf{n} \quad (3.14)$$

$$\boldsymbol{\kappa} - (\boldsymbol{\kappa} \cdot \mathbf{n})\mathbf{n} = 0 \quad (3.15)$$

$$\mathbf{u} \cdot \mathbf{n} = 0 \quad (3.16)$$

Where the components of  $\boldsymbol{\kappa}$  are the Lagrange multipliers used to implement the slip boundary condition,  $\mu$  is the fluid dynamic viscosity,  $\mathbf{n}$  is the boundary normal pointing out of the domain, and  $\mathbf{u}$  is the fluid velocity.

### 3.5. Model Computational Scheme

To assess the effects of aperture anisotropy on flow and heat transfer processes, model runs are completed with variable flow orientation. Inlet and outlet positions are altered between each model run such that each of the two possible flow orientations are modeled in the forward and reverse directions. In total, flow is modeled through each aperture in the positive X direction, negative X direction, positive Y direction, and negative Y direction for a total of four orientations.

Additionally, upscaling of model results may be performed via dimensional analysis and use of variable inlet velocities. While the model domain utilized in this study is small, heat and flow solutions within a larger model domain with upscaled roughness features may be simulated while utilizing the same model geometry dimensions via use of the Peclet number. The dimensionless Peclet number is the ratio of advective heat transport to diffusive heat transport, and may be calculated with the following equation:

$$Pe = \frac{U * L}{\alpha} \quad (3.17)$$

Where  $U$  is the mean aperture fluid velocity,  $L$  is the characteristic length dimension or half of the aperture width, and  $\alpha$  is the thermal diffusivity of water. Larger Peclet numbers are characteristic of larger fracture systems where advective heat transport dominates. This effect can be replicated within a smaller model domain via an increase in the mean flow velocity. Thus, for each flow orientation sampled, variable inlet velocities are applied spanning three orders of magnitude (Table 3.1). Due to the variable flow velocities and orientations sampled, 144 model runs are completed in total to generate the data presented in Chapter 4.

### 3.6. Output Processing

Temperature and fluid flow data were acquired for each steady state model simulation through the use of model probes in COMSOL®. Boundary probes were used to acquire data on the following: (1) mean heat flux magnitude on the upper and lower fracture interfaces (W) (Figure 3.2-C), (2) inlet and outlet fluid temperature (°C) (Figure 3.2-A,B), (3) inlet and outlet volumetric fluid flux (m<sup>3</sup>/s), and (4) inlet and outlet fluid pressure (Pa). Domain probes were used to acquire average fluid velocity (m/s) within the fracture domain (Figure 3.1-A). Probe data was exported to MATLAB® for evaluation and post-processing.

The effective hydraulic aperture was calculated for all model runs via use of probe data from the Stokes flow solution and the rearranged form of the cubic law (Eq. 1.11) for parallel plate flow [34]:

$$b_{eff} = \sqrt[3]{\frac{Q}{W} \frac{12\mu}{\rho g} \frac{L}{\Delta h}} \quad (4.1)$$

Where  $b_{eff}$  (m) is the hydraulic aperture,  $Q$  (m<sup>3</sup>/s) is the volumetric fluid flux,  $W$  (m) and  $L$  (m) are the width and length of the fracture plane,  $\mu$  (Pa · s) and  $\rho$  (kg/m<sup>3</sup>) are the dynamic viscosity and density of the fluid, and  $\Delta h$  (-) is the hydraulic head gradient between the fracture inlet and outlet. Results from these calculations are shown in

Table 4.1.

Shear-displacement of fracture surfaces causes the mean aperture width to deviate from the initial 0.5 mm width. Because the mean fracture surface heat flux is sensitive to the mean fracture aperture, models were made for the purpose of normalization so that outputs from models with differing mean apertures may be compared directly. Three parallel plate normalization models were made in COMSOL® with aperture widths equal to the mean

aperture width value for the shear displaced  $H = 0.75_{\text{HET}}$ ,  $0.90_{\text{HET}}$ , and  $0.93_{\text{HET}}$  models (Table 3.2). Output heat flux from the shear-displaced models were divided by the heat flux magnitudes from corresponding parallel plate models at all modeled inlet velocities to achieve normalization (Figure 4.8).

### 3.7. Tables

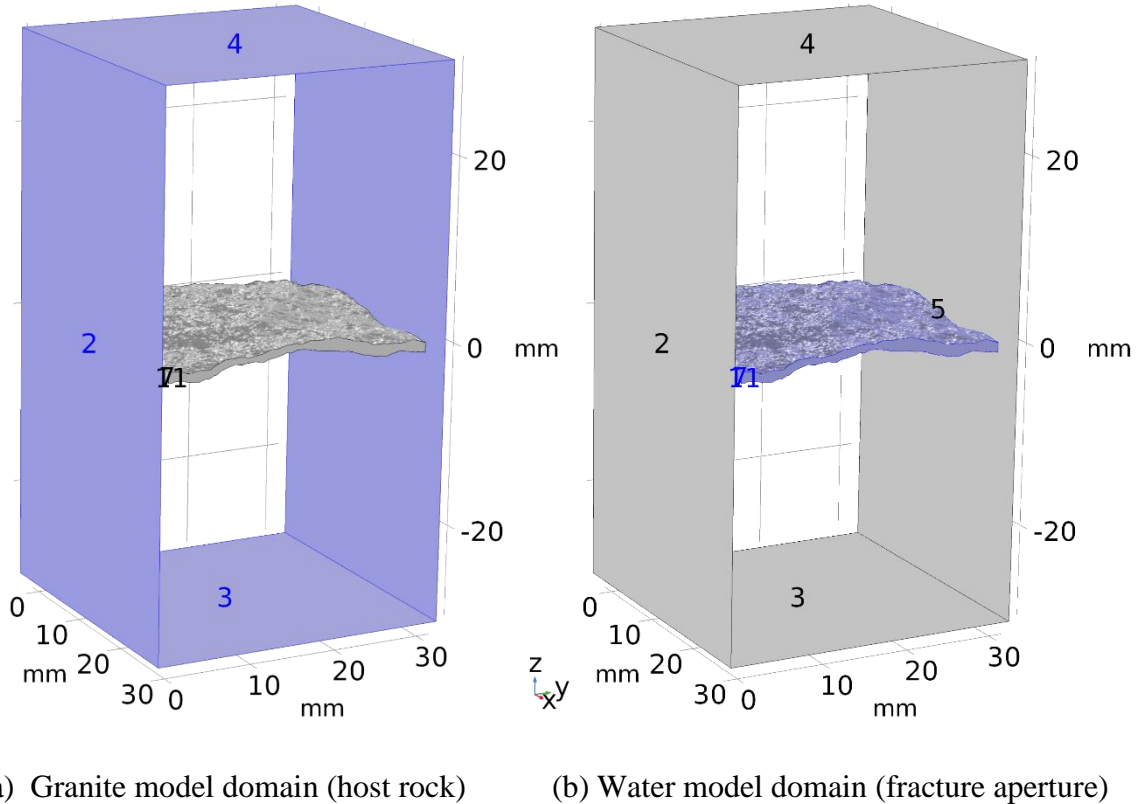
Table 3.1. Parameters and boundary conditions utilized in COMSOL simulations

Parameter	Unit	Value
Initial granite temperature (initial guess for steady state)	°C	90.0
Initial fluid temperature	°C	25.0
Granite boundary temperature	°C	92.5
Upstream temperature	°C	25.0
Initial upstream pressure	$p(\text{kPa})$	101.3
Outlet pressure	$p(\text{kPa})$	0
Inlet velocity	cm/s	0.01, 0.1, 1.0, 3.0, 5.0, 10.0
Hydrodynamic entrance length	cm	0
Water dynamic viscosity	$\mu(\text{Pa} \cdot \text{s})$	8.925E-4
Water density	$\rho(\text{kg}/\text{m}^3)$	967.75

Table 3.2. Apertures used for COMSOL modeling with surfaces implemented and standard statistics denoted. Subscript <sub>HOM</sub> refers to homogeneous aperture due to no fracture surface shear, subscript <sub>HET</sub> refers to heterogeneous apertures produced by X-direction surface shear.

Aperture Model	Surface Used	Surface Shear [mm]	Mean Aperture Width [mm]	Aperture Variance [mm <sup>2</sup> ]	Asperity Area [%]
$H = 0.93_{\text{HOM}}$	SG-002 Lower	0	0.500	0	0
$H = 0.93_{\text{HET}}$	SG-002 Lower	1.5	0.707	0.065	5.094
$H = 0.90_{\text{HOM}}$	Synthetic H=0.90	0	0.500	0	0
$H = 0.90_{\text{HET}}$	Synthetic H=0.90	1.5	0.667	0.069	6.735
$H = 0.75_{\text{HOM}}$	Synthetic H=0.75	0	0.500	0	0
$H = 0.75_{\text{HET}}$	Synthetic H=0.75	1.5	0.729	0.092	7.331

### 3.8. Figures



(a) Granite model domain (host rock)

(b) Water model domain (fracture aperture)

Figure 3.1: Composite image of the COMSOL® fracture model containing the H=0.90 synthetic fracture. A. Granite domain with diffusive-only transport, with front and back faces removed for visibility of fracture; B. Fracture domain with advective-diffusive transport and creeping flow.

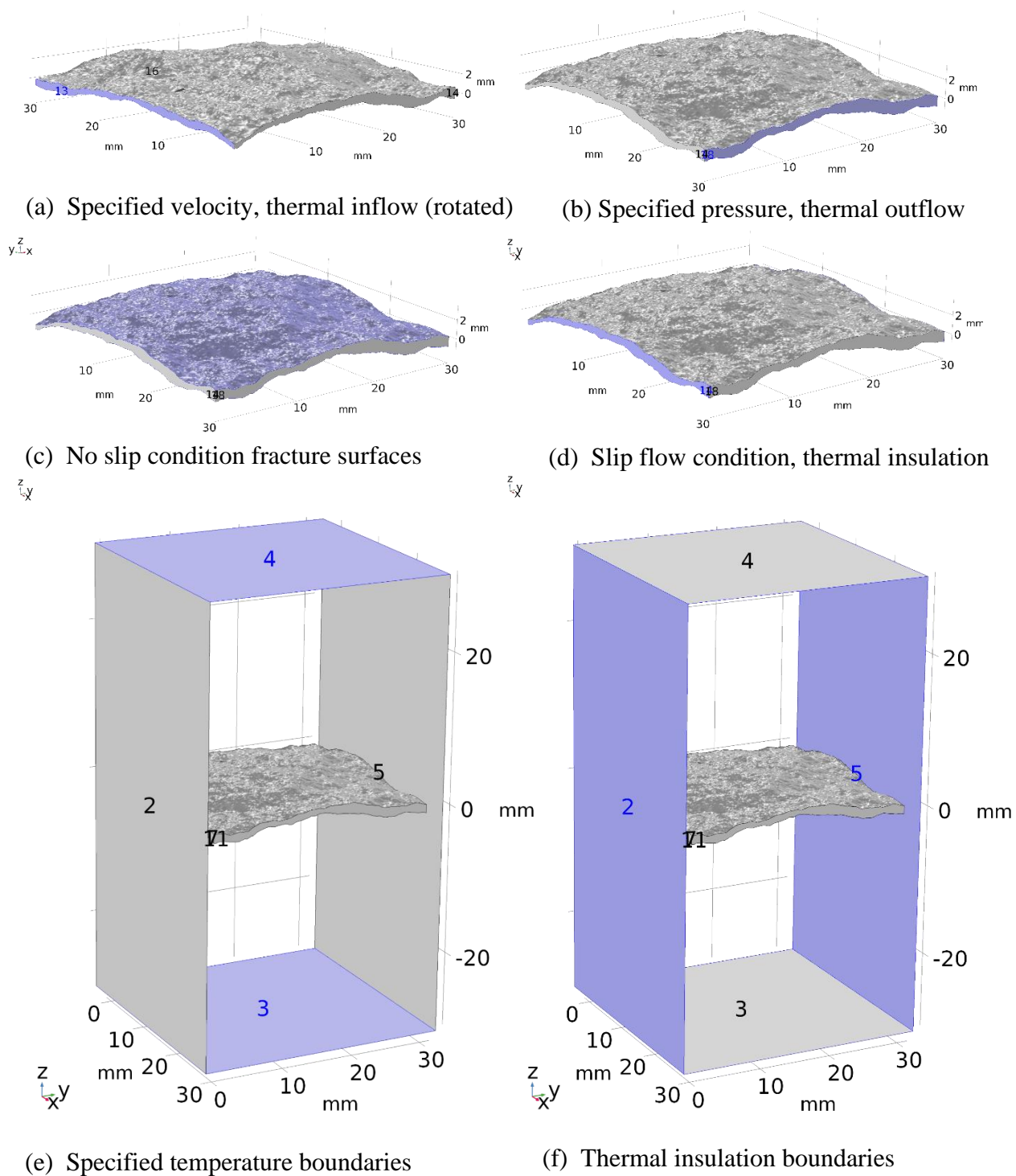


Figure 3.2 A-F. Composite image of the 1.5 mm sheared  $H = 0.90$  COMSOL® fracture model with dimensions and physics for reference. Five other COMSOL® models were made, not shown, for the cases of sheared and non-sheared  $H = 0.75, 0.90$ , and  $H \approx 0.93$  (natural) fracture surface roughness (Table 3.2). Note the 90° rotated orientation of (a) for visualization.

## 4. Results

Steady-state numerical model outputs from COMSOL were extracted for quantitative analysis. Key observations such as the effective hydraulic aperture, magnitude of fracture surface heat transfer, and the fracture outlet fluid temperature were determined to assess differences in flow and heat transfer behavior across models of variable surface roughness and aperture heterogeneity. The effect of variable surface roughness between models was isolated through direct comparison of homogeneous 0.5 mm aperture model outputs ( $H = 0.75_{\text{HOM}}$ ,  $0.90_{\text{HOM}}$ ,  $0.93_{\text{HOM}}$ ). The added effect of aperture heterogeneity on parameters of interest was quantified through comparison of the shear-displaced models ( $H = 0.75_{\text{HET}}$ ,  $0.90_{\text{HET}}$ ,  $0.93_{\text{HET}}$ ). The following analysis aims to identify relationships between geospatial mechanical aperture measurements, flow, and heat transfer behaviors through comparison of model outputs.

### 4.1. Model Output

#### 4.1.1. Numerical Model Validation

To ensure the validity of results from the modeling work conducted in this thesis, numerical model outputs for flow and heat transfer were compared with a simplified analytical solution. The 1-dimensional analytical solution to flow and heat transfer between parallel plates from Zhao 2014 was chosen for output comparison [32]. This solution neglects thermal diffusion within the fluid and assumes that the temperature at the rock fracture surface is the same as that of the bulk fluid. Boundary conditions of the analytical solution specify that the fluid temperature at the inlet  $T_{in}$  is constant, the temperature of the rock at distance  $R$

perpendicular to the fracture plane is constant, and the temperature of the fluid at an infinite distance from the inlet  $T_f(x = \infty)$  is equal to that of the rock  $T_0$ . The equation for fluid temperature along the fracture plane  $T_f(x)$  is therefore:

$$T_f(x) = T_0 + (T_{in} - T_0) \cdot \exp\left(-x \frac{k_r}{v\rho_w C_w b R}\right) \quad (4.2)$$

Where  $x$  (m) is the distance from the inlet along the fracture plane,  $T_0$  ( $^{\circ}$ C) is the rock temperature at distance  $R$  (m) from the fracture plane,  $T_{in}$  ( $^{\circ}$ C) is the fluid temperature at the fracture inlet,  $k_r$  (W/m · K) is the thermal conductivity of granite,  $b$  (m) is the half aperture width of the fracture, and  $\rho_w$  (kg/m<sup>3</sup>),  $C_w$  (J/kg · K),  $v$  (m/s) are the density, specific heat capacity, and steady flow velocity of the fluid. Equation 4.2 was used to obtain analytical outlet temperatures within a parallel plate domain possessing a constant 0.5 mm aperture given a sweep of inlet temperatures (Table 4.2). For the most direct comparison, outlet temperatures from the non-shear displaced numerical models possessing a mean aperture of 0.5 mm were compared to the analytical solution outputs. Generally, numerical outlet temperatures compare favorably with the analytical solution, however RMSE error increases with fracture surface roughness as may be expected with deviation from a parallel plate geometry (Figure 4.7).

## 4.2. Analysis of Results

### 4.2.1. Aperture Heterogeneity and Flow

Figures Figure 4.1, Figure 4.2, and Figure 4.3 A-B show the steady state Stokes flow solution with streamlines viewed in the X-Y plane for each modeled fracture aperture. In each image, streamlines are superimposed upon the aperture width distribution for reference, and the streamline width is proportional to the fluid velocity magnitude. In addition, the steady state pressure distribution is provided. Upon visual inspection, several trends in flow are observable. Generally, flow is channeled within sections of greater aperture width oriented parallel to the direction of flow. Within these channels flow velocities are greatest, and the local pressure gradient is at its minimum. Additionally, flow is diverted around asperities where present, and the orientation of asperities has a controlling effect on flow tortuosity. Flow exhibits maximum tortuosity when the long axis of asperities are oriented perpendicular to the direction of flow, while the opposite is true when asperities are oriented parallel to the direction of flow (Figure 4.2 A,B). Furthermore, significant pressure gradients along asperities are associated with reduced permeability and enhanced flow tortuosity and constriction. These observations are explored quantitatively in the following discussion.

The normalized hydraulic aperture (NHA) ( $b_{eff}/b_{mech}$ ) yields a quantitative metric of the reduction in fracture permeability relative to a parallel plate aperture due to aperture heterogeneity. Roughness and shear-induced aperture heterogeneity have been shown to decrease permeability and increase pressure loss via enhanced flow tortuosity, constriction, and impedance by asperities. The influence of these effects on the NHA is shown in Figures Figure 4.1, Figure 4.2, and Figure 4.3 A-B. Reduction of the NHA due to increased flow

tortuosity is best observed in Figures Figure 4.1 and Figure 4.2, A-B. In both solutions shown, flow in the X-axis parallel direction is characterized by qualitatively greater tortuosity and a reduced NHA relative to the Y-axis parallel flow solution. Reduction of the NHA due to flow constriction is best shown in Figure Figure 4.3 A-B. In this case, flow constriction in the Y-axis parallel direction caused by the presence of oblique asperities significantly reduces the NHA relative to X-axis parallel flow. This reduction is reflected by the significant pressure gradient along the low permeability asperity (Figure 4.3 A). Furthermore, NHA is qualitatively shown to be reduced as asperity orientation deviates from the direction of flow for all shear-displaced apertures. In the non-shear displaced apertures, flow paths are semi-linear due to aperture homogeneity and NHA generally correlates with surface smoothness, where rougher surfaces yield smaller NHA (Table 4.1). It is speculated that this is due to increased viscous boundary layer thickness due to protruding surface roughness features as shown in Figure 4.10 A-C.

While the NHA provides an informative bulk parameter estimating relative pressure loss due to aperture heterogeneity, its value is limited by the need to fully characterize and model each aperture individually. Predictive relationships between spatial measurements of mechanical aperture characteristics and resulting fluid flow behaviors are thus more valuable. In this regard, geostatistical measurements of the mechanical apertures in this thesis have yielded useful correlations to flow behaviors. The aperture width correlation length ( $\xi$ ) parallel to the direction of flow is shown to generally predict flow tortuosity, with shorter  $\xi$  corresponding to more tortuous flow. Consequently, when submitted to equal inlet and outlet boundary conditions, flow parallel to the longer  $\xi$  is characterized by greater mean flow velocity and Peclet numbers (Table 4.1). It is speculated that reduced aperture variability in

the direction of flow as indicated by longer  $\xi$  is favorable for the formation of strongly advective flow channels.

#### *4.2.2. Flow and Heat Exchange Characteristics*

Figures Figure 4.4, Figure 4.5, and Figure 4.6 A-F show the steady state heat flux magnitudes across the fracture interface from the granite to the fluid domain as viewed in the X-Y plane for each modeled aperture. The steady state solutions are shown in both sampled flow orientations for three of the six inlet velocities modeled spanning three orders of magnitude, corresponding to 0.1, 1.0, and 10.0 cm/s. When comparing the streamline solution (Figures Figure 4.1, Figure 4.2, and Figure 4.3 A-B) to the coupled heat transport solution (Figures Figure 4.4, Figure 4.5, and Figure 4.6 A-F) it can be observed that the greatest heat flux occurs along strongly advective flow channels. Additionally, it can be observed that the mean magnitude of heat flux increases with fracture surface Hurst exponent (increased smoothness) and advective velocity. While not shown, the modeled fracture apertures with no shear displacement exhibit lower mean fracture interface heat flow due to smaller aperture widths relative to shear displaced models. However, non-shear displaced models exhibit the same positive correlation in heat flux magnitude and fracture surface Hurst exponent (Table 4.1).

As discussed in the previous section, (1) surface roughness and (2) aperture heterogeneity strongly influence flow characteristics within fractures. Accordingly, flow characteristics control the efficiency of heat exchange between fracture fluids and the host rock. The effect of fracture surface roughness on heat exchange efficiency in the absence of

aperture heterogeneity was isolated via modeling of flow and heat transfer within uniform-aperture rough-walled fractures. Figure 4.9 shows the mean fracture surface heat flow magnitude plotted as a function of flow Peclet number for the non-shear displaced fracture aperture models. It is observed that surface roughness as measured by the surface Hurst exponent decreases heat exchange efficiency between the fracture surface and fluid. It is speculated that surface roughness thickens the viscous boundary layer at the fracture surface thereby increasing the distance through which diffusive exchange must occur and decreasing the efficiency of advective heat transport to the fracture outlet. This is best observed in Figure 4.10 A-C, which shows representative aperture cross sections with calculated Peclet number from each non-shear displaced model ( $H = 0.75_{\text{HOM}}, 0.90_{\text{HOM}}, 0.93_{\text{HOM}}$ ) under variable flow velocity conditions. It can be seen qualitatively that the width of central high Peclet number channel is diminished in the  $H = 0.75_{\text{HOM}}$  (Figure 4.10 C) relative to the smoother  $H = 0.90_{\text{HOM}}$  and  $H = 0.93_{\text{HOM}}$  models (Figure 4.10 A-B). While surface roughness alone lessens heat exchange efficiency, aperture heterogeneity is another important morphological factor to consider.

Figure 4.8 A-B shows the fracture surface heat flow normalized by the parallel-plate heat flow as a function of flow Peclet number within the heterogeneous shear-displaced fracture apertures ( $H = 0.75_{\text{HET}}, 0.90_{\text{HET}}, 0.93_{\text{HET}}$ ). Heat flow normalization is implemented so that heat exchange magnitudes from heterogeneous models possessing different mean aperture widths may be compared directly. It is observed that variability in heat flow caused by aperture heterogeneity is most apparent at low flow Peclet numbers. At high Peclet numbers variability in heat flow collapses toward a common value for all models. This trend is inferred to be due to the relative importance of diffusion-dominated heat exchange at low Peclet numbers, where

viscous boundary layer thickness tends to be proportional to surface roughness features (Figure 4.10). At high Peclet numbers however, advective heat exchange dominates, viscous boundary layers thin due to increased flow velocity, and surface roughness exerts less influence on overall heat exchange.

Figure 4.11 A-C shows the non-normalized fracture surface heat flow as a function of flow Peclet number for each heterogeneous shear-displaced fracture aperture. Each frame shows the resultant heat flow in the X-parallel and Y-parallel flow directions with the aperture width correlation length  $\xi$  in the flow direction denoted for reference. It is shown that overall heat exchange efficiency exhibits anisotropy which is dependent upon the flow direction and the aperture width correlation length in the direction of flow. Longer aperture width correlation length is shown to correlate to greater fracture surface heat flow. It is again inferred that reduced aperture variability in the direction of flow favors the development of strong advective channels, and thus increased heat exchange with the host rock.

### 4.3. Primary Findings

Fluid flow and heat exchange within heterogeneous fractured rock has been the subject of decades of study, and while the findings stated here are consistent within the small sample size investigated, further experimentation is necessary to assess their validity within diverse geologic media. Nevertheless, primary findings from the work conducted in this thesis may be summarized as follows.

Within the constant width, rough-walled apertures modeled, flow and heat exchange behaviors deviate from the assumptions of the parallel plate model in the following ways: (1) Under laminar flow conditions, surface roughness increases pressure dissipation and decreases hydraulic aperture due to increased viscous effects from the fracture walls; (2) Surface roughness is negatively correlated with heat exchange efficiency due to reduced flow Peclet number near the fracture interface, within these zones inefficient diffusive heat transport dominates.

Within rough-walled heterogeneous apertures, flow and heat exchange behaviors deviate further from the assumptions of the parallel plate model: (3) Asperity orientation relative to flow direction is shown to have a controlling effect on hydraulic aperture and flow tortuosity, where asperities oriented perpendicular to flow produce maximum flow tortuosity and pressure dissipation; (4) It is shown that overall heat exchange efficiency exhibits anisotropy which is dependent upon the aperture width correlation length in the direction of flow. Within a heterogeneous aperture, the formation of strongly advective flow channels in the direction of longest correlation length facilitates enhanced heat exchange. In contrast, flow in the direction of shortest correlation length exhibits minimal heat exchange and maximum

tortuosity. (5) Additionally, surface roughness is shown to decrease mean correlation length and therefore heat exchange efficiency within a heterogeneous aperture.

## 4.4. Tables

Table 4.1. Normalized hydraulic aperture, aperture width correlation length, mean Peclet number, and mean interface heat flow calculated at 1 cm/s inlet velocity and averaged in both flow directions. Note: Natural surface corresponds to  $H = 0.93$  models.

Surfaces Used	Shear displace- ment [mm]	Flow orientation [axis, °]	$b_{eff}/b_{mech}$ [-]	Aperture Correlation length $\xi$ [mm]	Mean Peclet number [-]	Mean heat flow magnitude [W]
$H = 0.93_{HOM}$	0	X, 180	0.393	-	12.211	1.06E-04
$H = 0.93_{HOM}$	0	Y, 90	0.370	-	12.384	1.04E-04
$H = 0.93_{HET}$	1.5	X, 180	0.278	7.70	21.030	8.07E-04
$H = 0.93_{HET}$	1.5	Y, 90	0.215	11.91	22.839	9.34E-04
$H = 0.90_{HOM}$	0	X, 180	0.415	-	11.306	7.91E-05
$H = 0.90_{HOM}$	0	Y, 90	0.415	-	11.325	7.96E-05
$H = 0.90_{HET}$	1.5	X, 180	0.222	9.06	23.560	7.95E-04
$H = 0.90_{HET}$	1.5	Y, 90	0.316	7.36	22.167	7.08E-04
$H = 0.75_{HOM}$	0	X, 180	0.276	-	12.421	1.98E-05
$H = 0.75_{HOM}$	0	Y, 90	0.277	-	12.447	1.99E-05
$H = 0.75_{HET}$	1.5	X, 180	0.242	3.09	25.805	5.49E-04
$H = 0.75_{HET}$	1.5	Y, 90	0.289	5.73	28.247	6.60E-04

Table 4.2. Comparison of analytical and numerical fracture outlet temperatures for numerical model validation. Root-mean-squared-error (RMSE) calculated relative to the ‘Analytical Parallel Plate Solution’. See Figure 4.7 for the graphical representation of this data with the addition of the numerical rough-walled homogeneous aperture model solution outputs.

Analytical Parallel Plate Solution (Zhao 2014)	$T_{in}$ [°C]	$T_{out}$ [°C]	Numerical Model  COMSOL Parallel Plate Model	$T_{in}$ [°C]	$T_{out}$ [°C]
	45	86.154		45	85.354
	55	87.490		55	86.850
	65	88.826		65	88.363
	75	90.162		75	89.867
	85	91.498		85	91.372
	90	92.166		90	92.124
			RMSE [°C]	0.478	

## 4.5. Figures

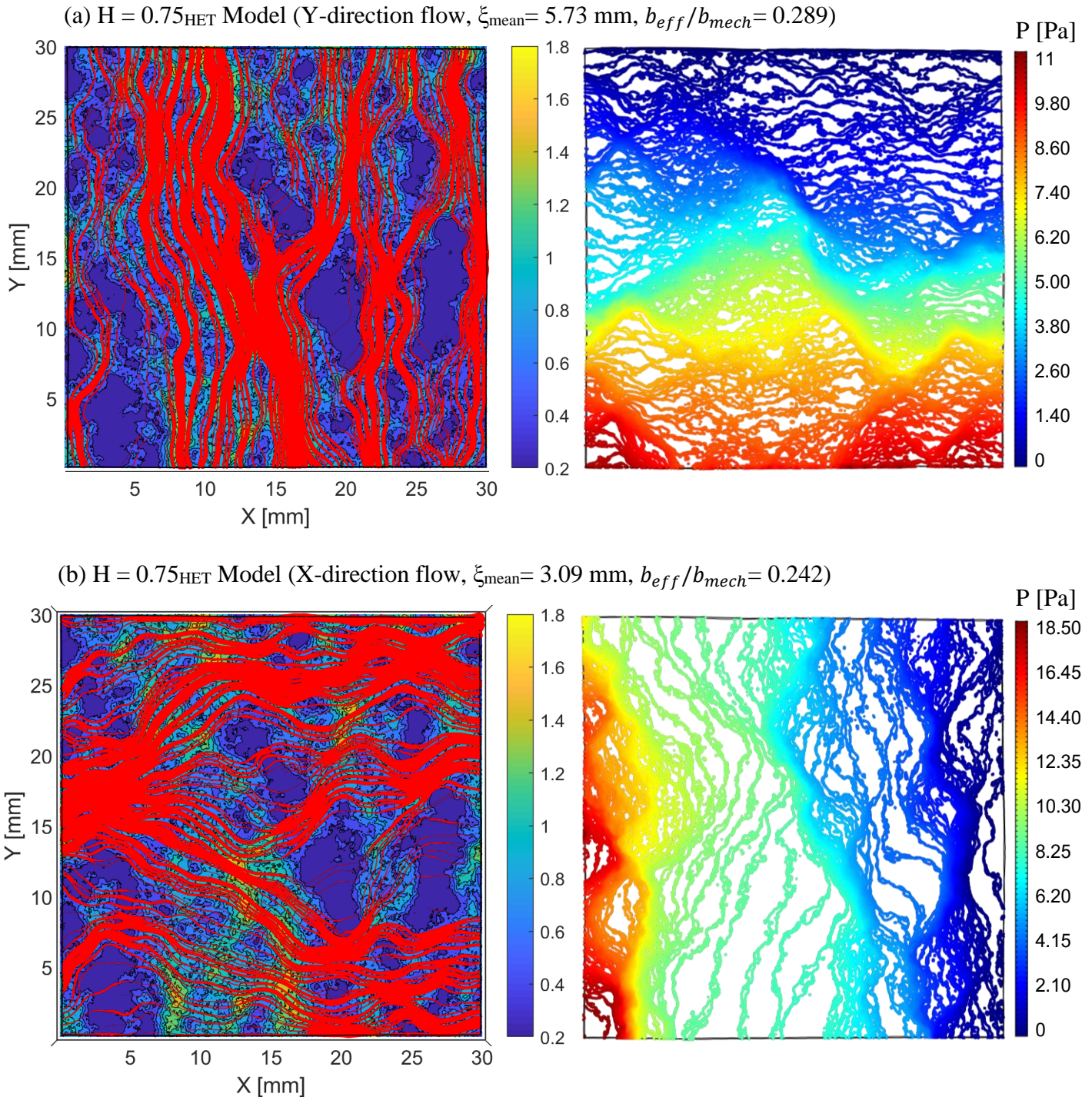


Figure 4.1 A,B. Streamlines solved via Stokes flow (left) in 1.5 mm shear displaced  $H = 0.75_{\text{HET}}$  aperture for variable flow orientations. Streamlines are superimposed upon aperture width distribution [mm]. Streamline thickness is proportional to flow velocity. Pressure isobars shown (right) illustrating local pressure gradient [Pa].

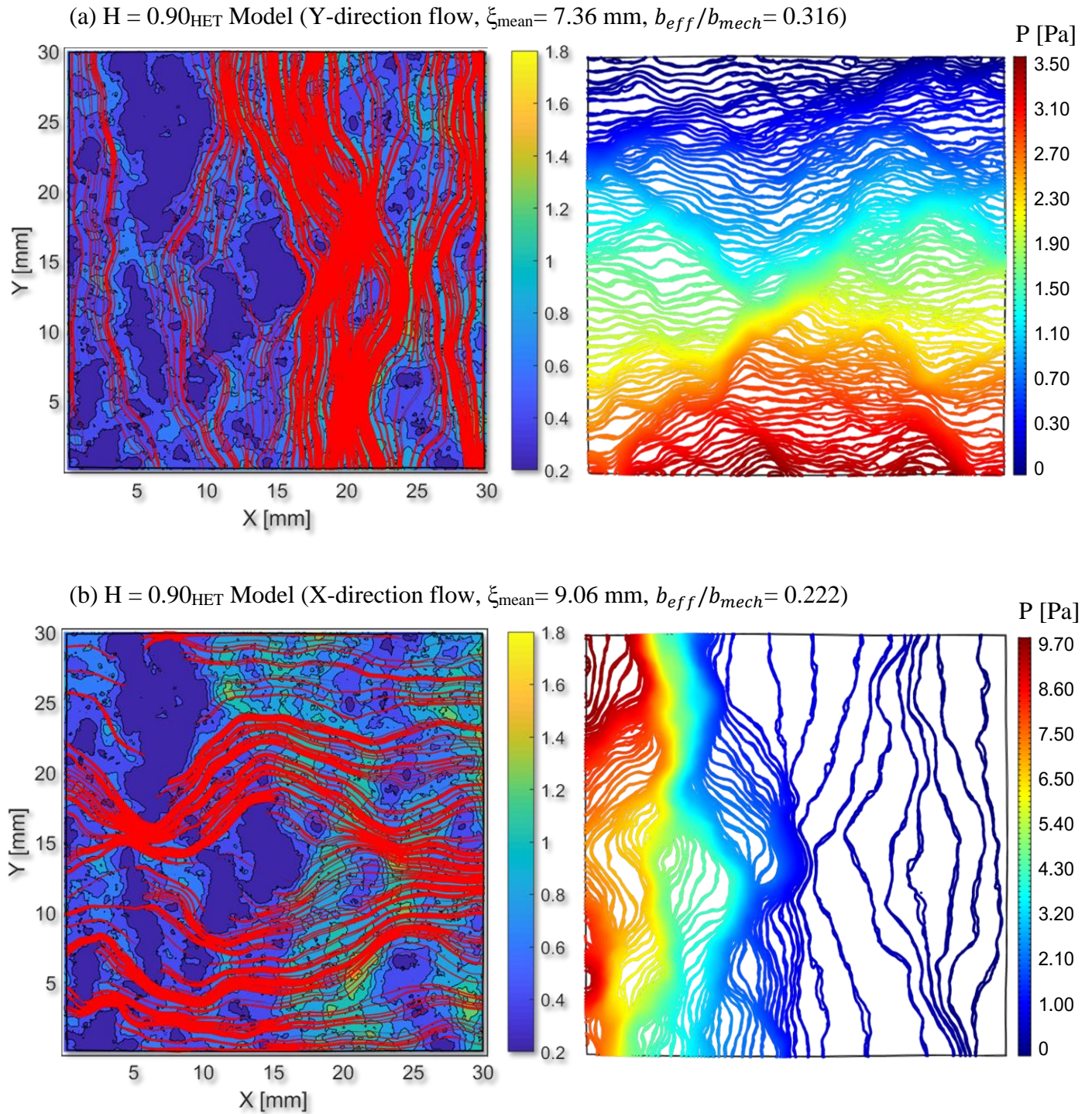


Figure 4.2 A,B. Streamlines solved via Stokes flow (left) in 1.5 mm shear displaced  $H = 0.90_{\text{HET}}$  aperture for variable flow orientations. Streamlines are superimposed upon aperture width distribution [mm]. Streamline thickness is proportional to flow velocity. Pressure isobars shown (right) illustrating local pressure gradient [Pa].

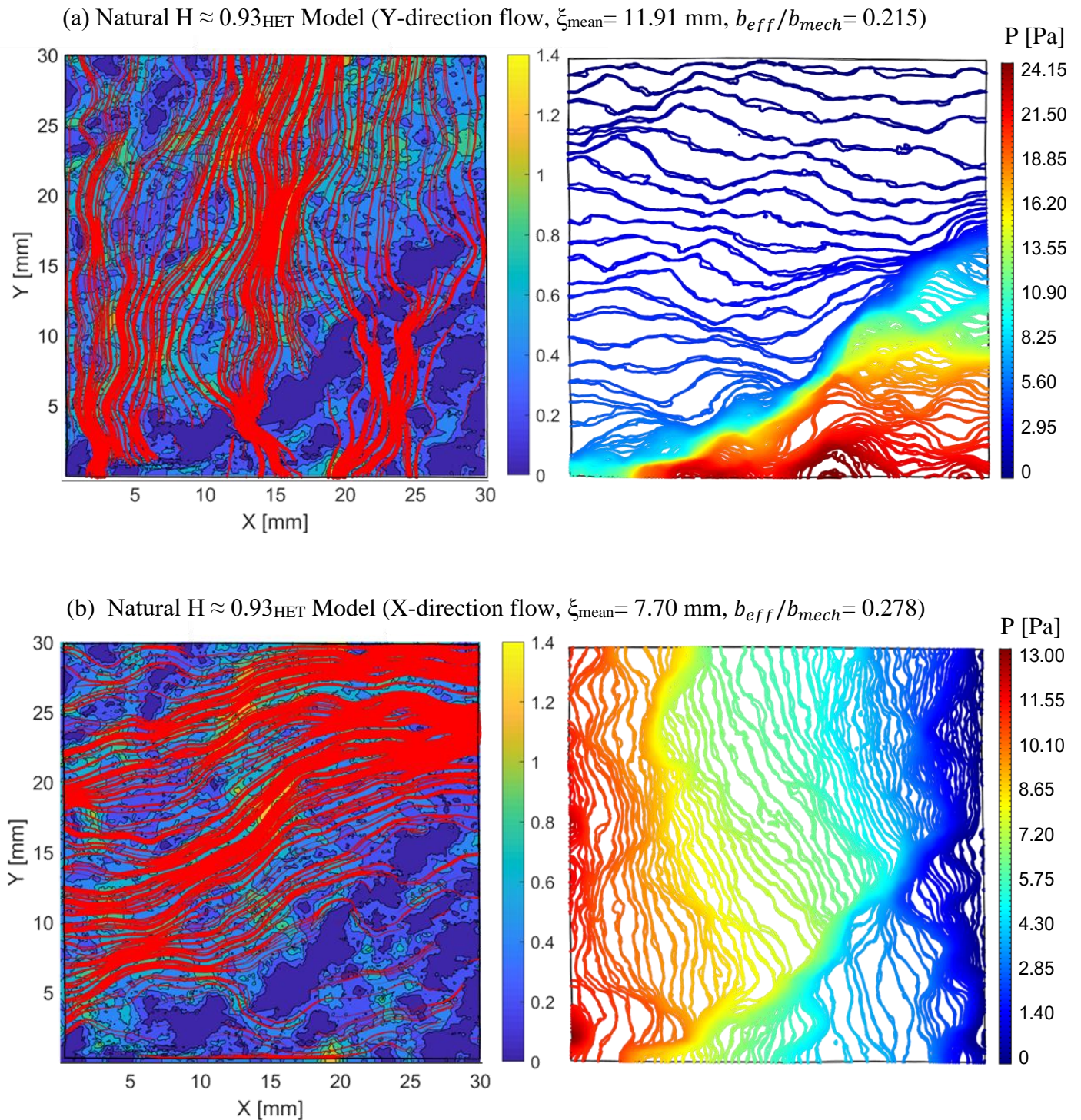


Figure 4.3 A,B. Streamlines solved via Stokes flow (left) in 1.5 mm shear displaced natural  $H = 0.93_{\text{HET}}$  aperture for variable flow orientations. Streamlines are superimposed upon aperture width distribution [mm]. Streamline thickness is proportional to flow velocity. Pressure isobars shown (right) illustrating local pressure gradient [Pa].

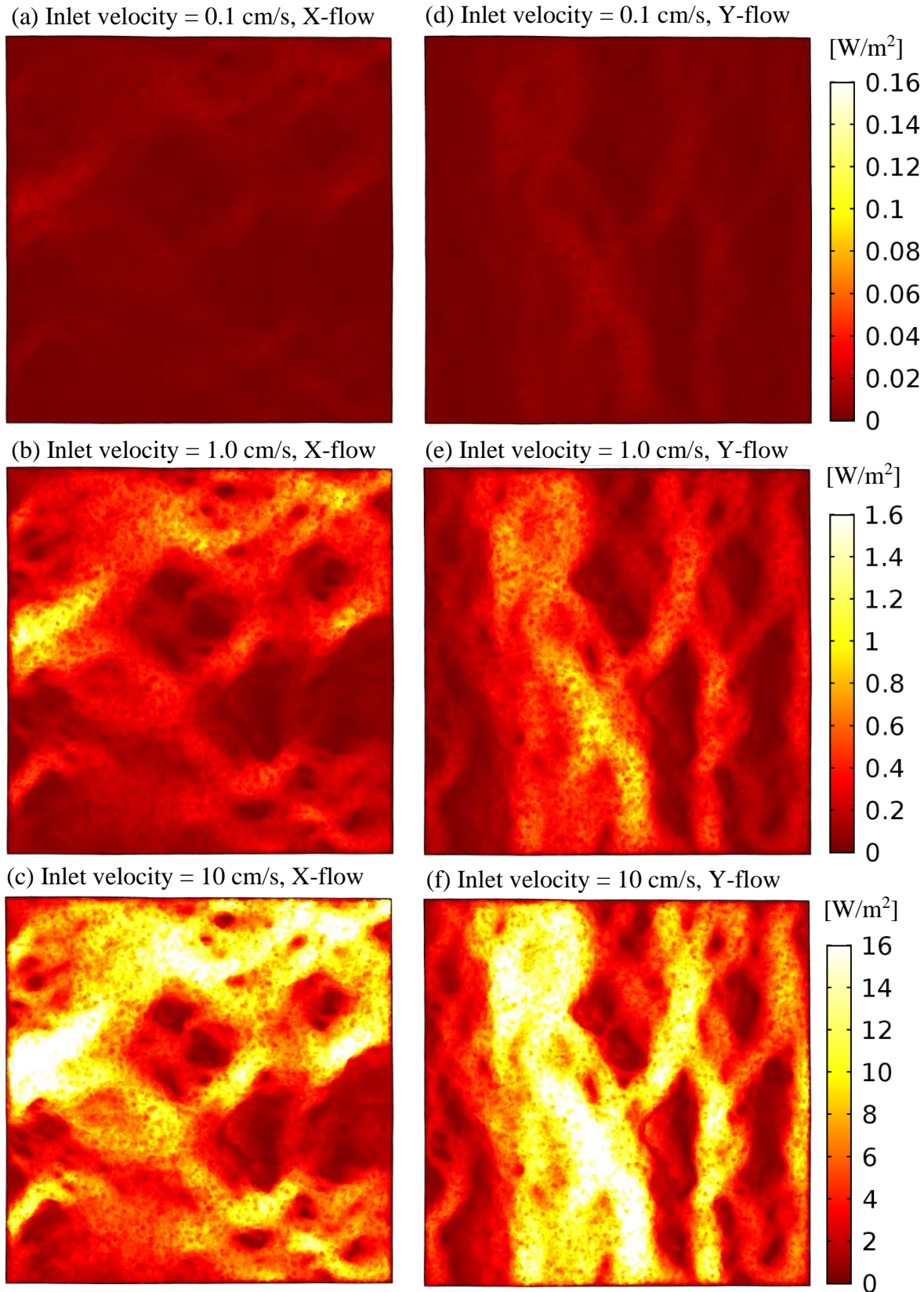


Figure 4.4 A-F. Heat flux magnitude across fracture interface  $[\text{W/m}^2]$  measured for 1.5 mm shear displaced  $H = 0.75$  HET model at variable flow orientations and inlet velocities.

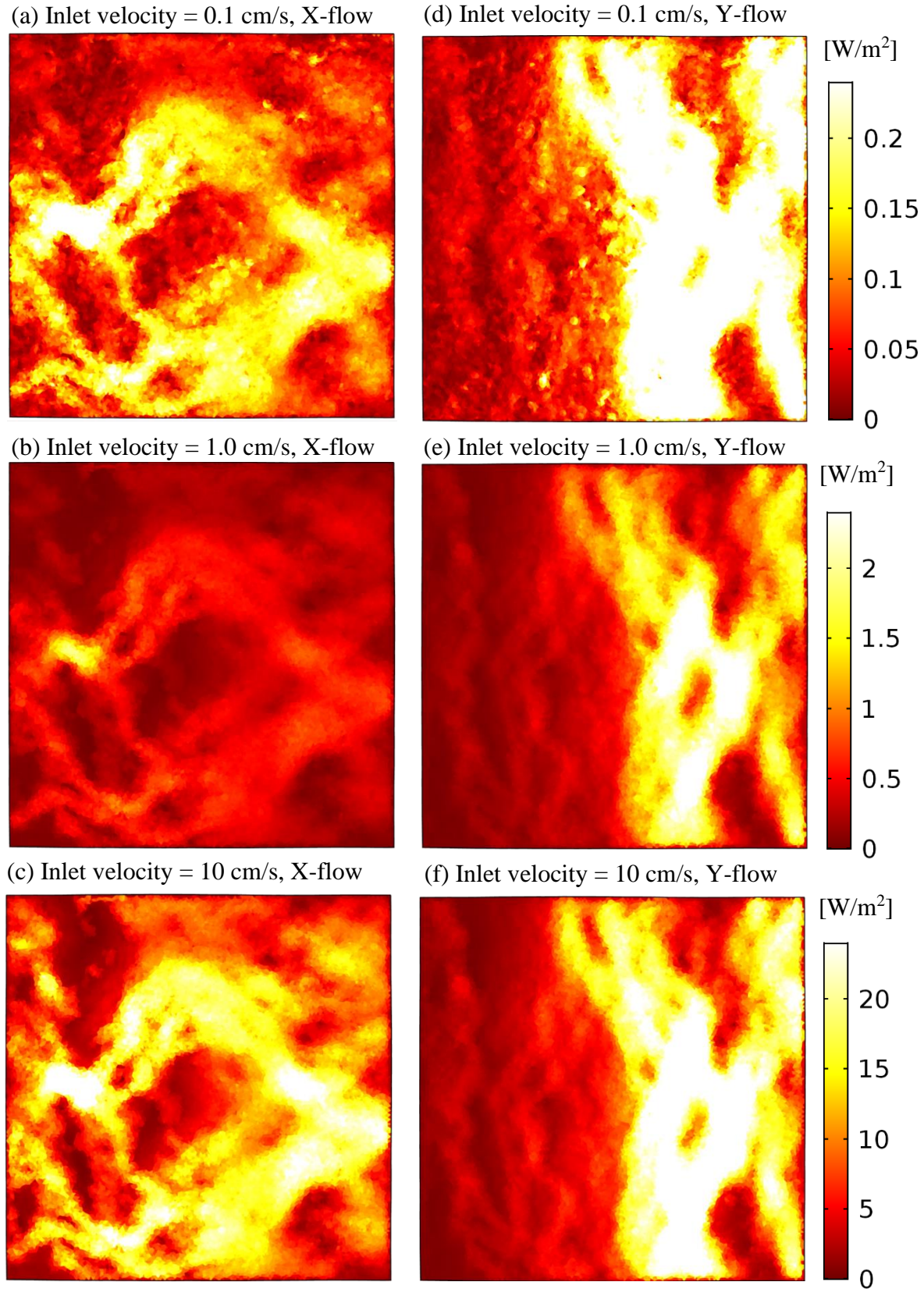


Figure 4.5 A-F. Heat flux magnitude across fracture interface [W/m<sup>2</sup>] measured for 1.5 mm shear displaced H = 0.90 HET model at variable flow orientations and inlet velocities.

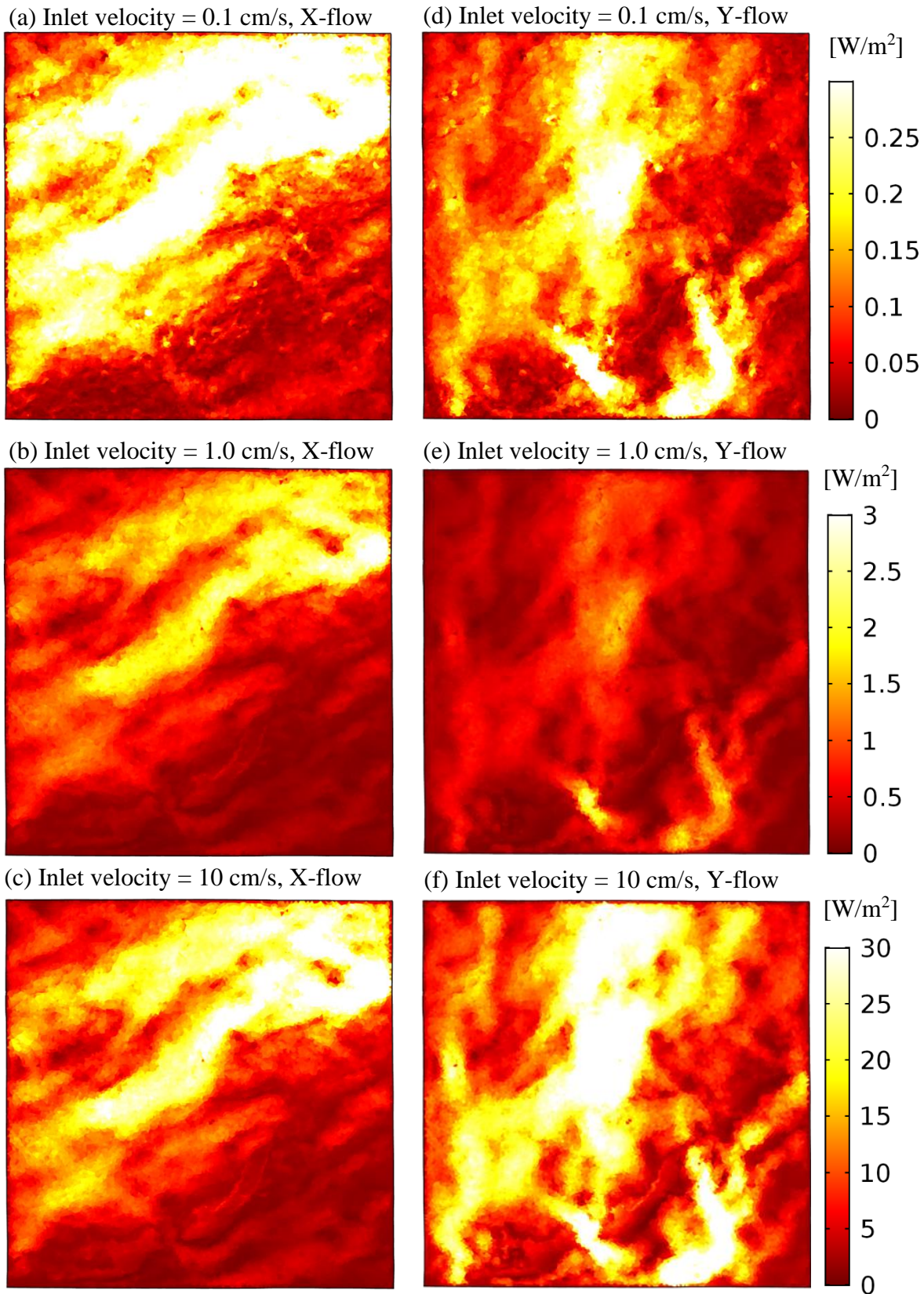


Figure 4.6 A-F. Heat flux magnitude across fracture interface [W/m<sup>2</sup>] measured for 1.5 mm shear displaced natural H  $\approx 0.93_{\text{HET}}$  model at variable flow orientations and inlet velocities.

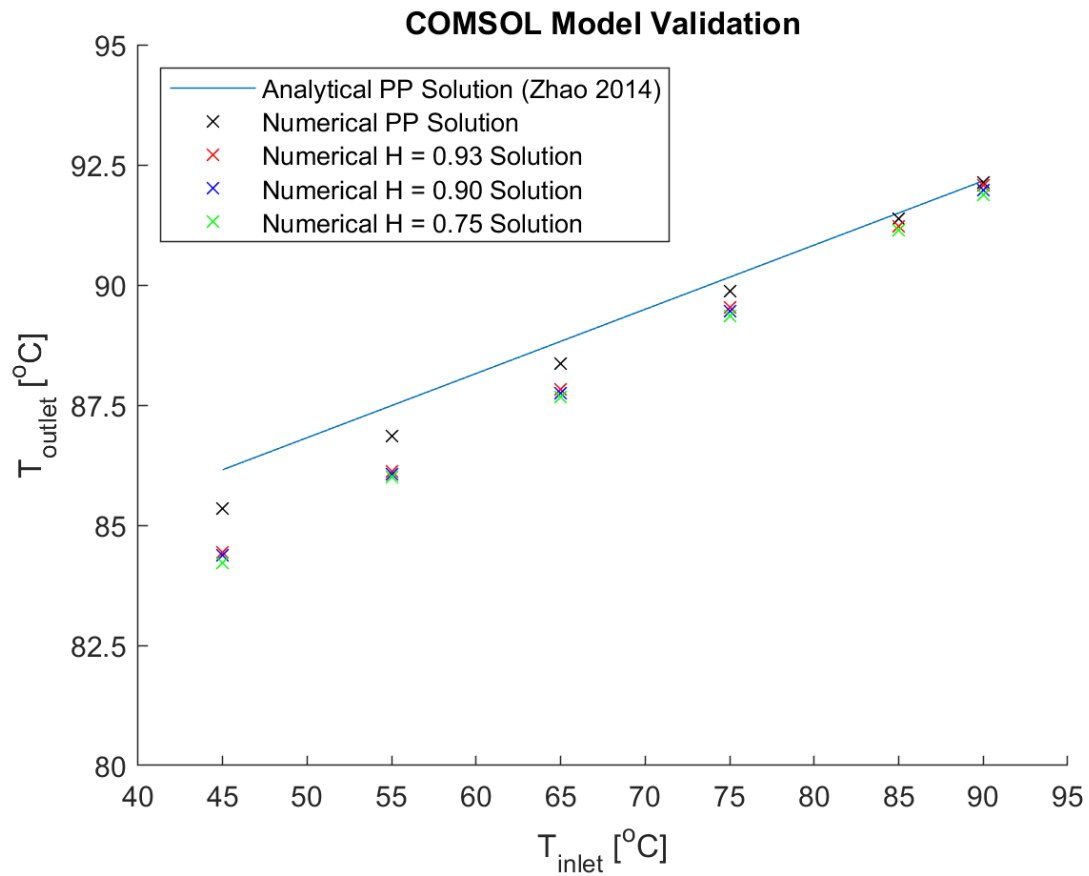


Figure 4.7 Comparison of numerical model outlet temperatures with the 1-dimensional analytical solution for flow between parallel plates. ‘Numerical PP Solution’ refers to the parallel plate FEM model built in COMSOL®. All models ( $H = 0.75_{HOM}$ ,  $0.90_{HOM}$ ,  $0.93_{HOM}$ ) possess a homogeneous 0.5 mm mean aperture width, but surfaces of variable roughness.

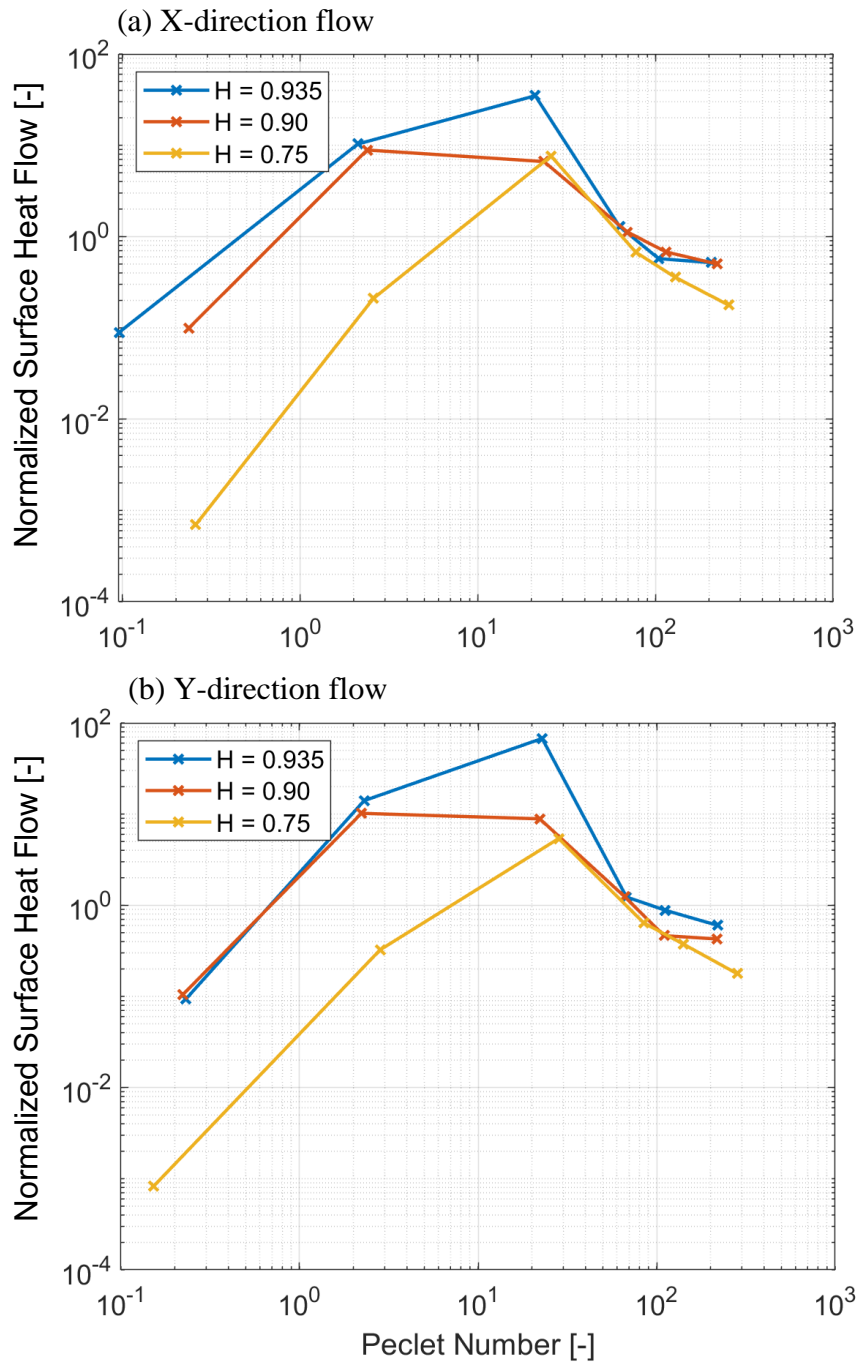


Figure 4.8 A-B. Parallel plate-normalized fracture surface heat flow magnitudes plotted as a function of flow Peclet number for the 1.5 mm shear-displaced  $H = 0.75_{\text{HET}}$ ,  $0.90_{\text{HET}}$ , and  $0.93_{\text{HET}}$  natural surface models. Data is shown for model runs in both the X and Y-axis parallel directions. It is observed that (1) variability in heat flux between models decreases with increased Peclet number, (2) heat flux decreases with surface roughness especially at low Peclet numbers.

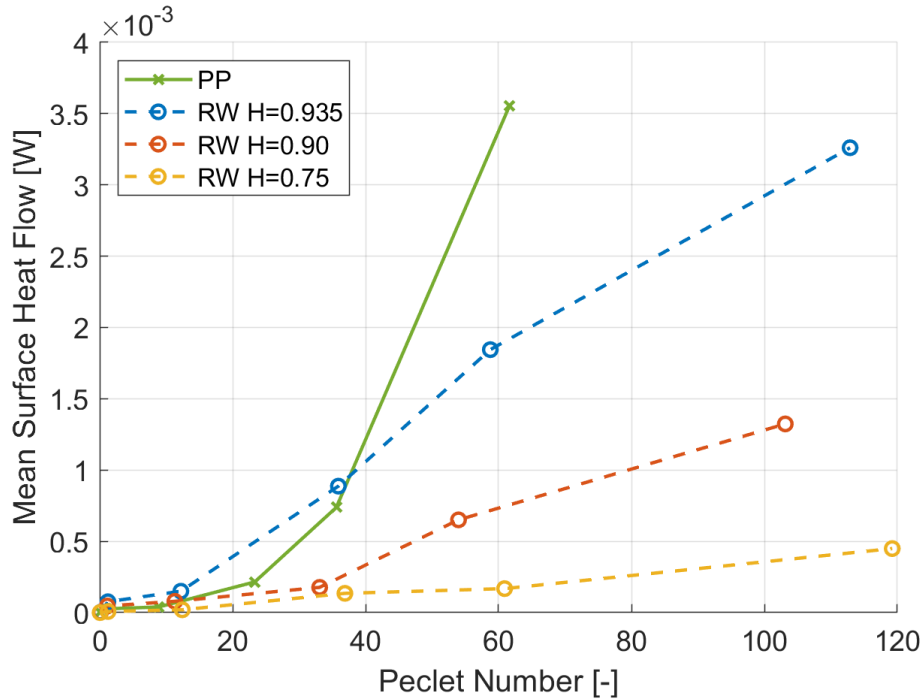


Figure 4.9. Mean fracture surface heat flow plotted as a function of flow Peclet number for the  $H = 0.75_{\text{HOM}}$ ,  $0.90_{\text{HOM}}$ ,  $0.93_{\text{HOM}}$  rough-walled 0.5 mm aperture (RW) models and the 0.5 mm aperture parallel plate (PP) numerical model.

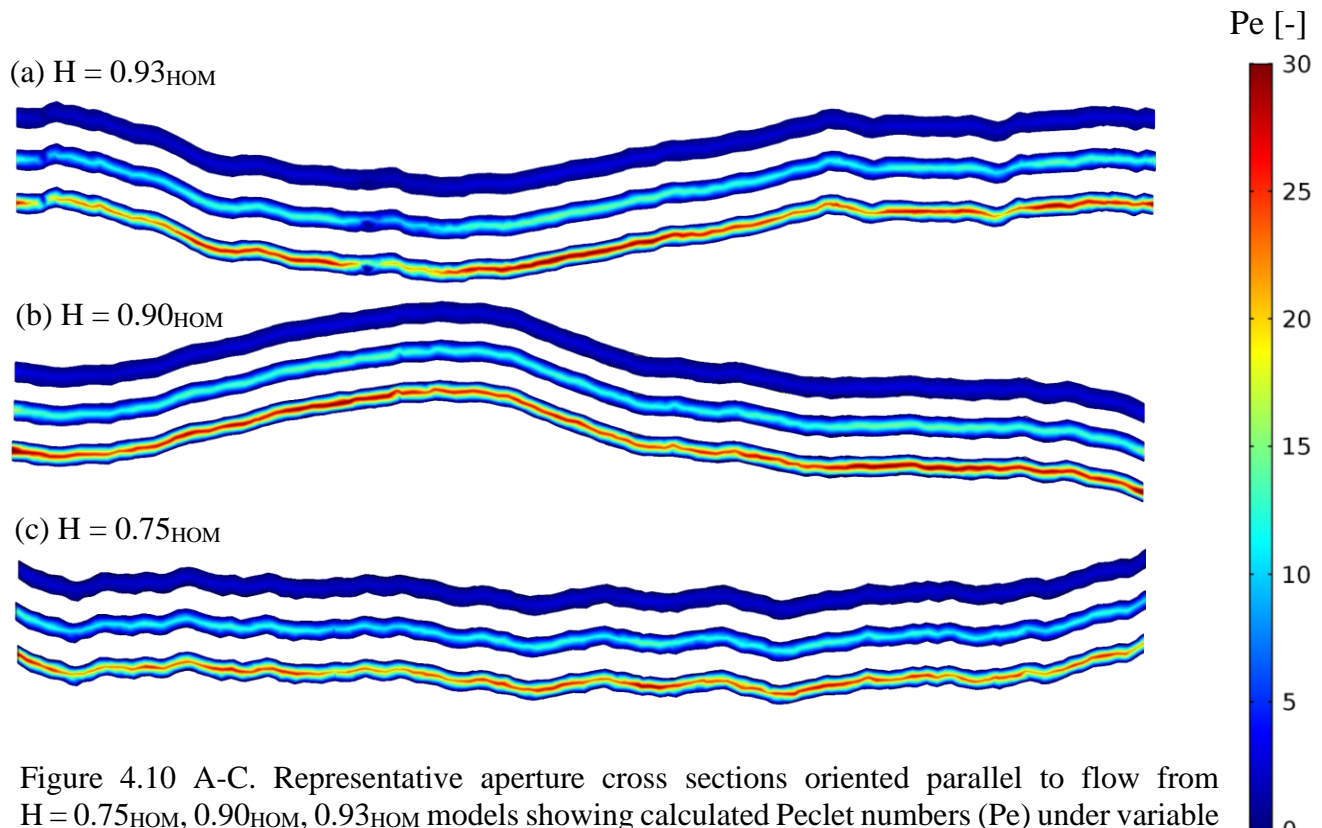


Figure 4.10 A-C. Representative aperture cross sections oriented parallel to flow from  $H = 0.75_{\text{HOM}}$ ,  $0.90_{\text{HOM}}$ ,  $0.93_{\text{HOM}}$  models showing calculated Peclet numbers (Pe) under variable inlet velocities; From top to bottom  $v_{\text{inlet}} = 0.1, 0.5, 1.0 \text{ cm/s}$ . It is observed that high Peclet channels develop more fully with decreasing roughness. Also, diffusive transport is shown to dominate at low Peclet numbers.

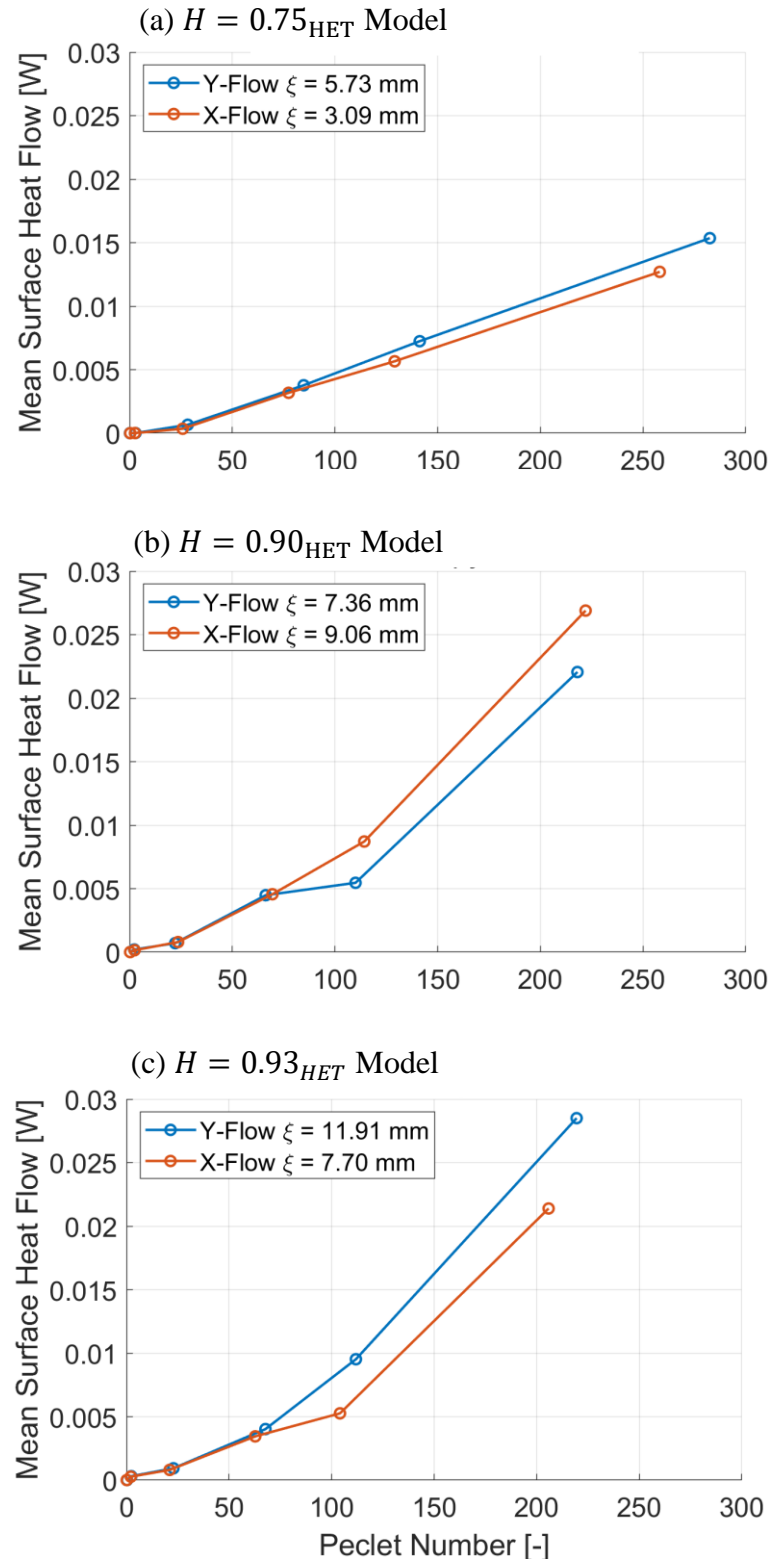


Figure 4.11 A-C. Illustration of heat flow anisotropy with flow direction and relation to aperture width correlation length ( $\xi$ ). Mean fracture heat flow is plotted as a function of flow Peclet number for 1.5 mm shear-displaced models. It is observed that longer aperture width correlation lengths correlate with enhanced heat flow especially at Peclet numbers  $> 60$ .

# 5. Conclusions and Future Work

## 5.1. Conclusions

Three-dimensional flow and energy exchange processes were simulated within a series of rough-walled natural and synthetic fracture apertures. Fracture surface roughness as measured by the surface Hurst exponent was found to reduce heat exchange efficiency and hydraulic aperture under laminar flow conditions, even without fracture displacement. It is speculated that this is due to the thickening of the diffusion-dominant viscous boundary layer between the fracture surface wall and the fully developed flow channel thereby impeding advective heat exchange. Spatial trends in fracture aperture heterogeneity were evaluated for the purpose of investigating the resulting flow and heat exchange characteristics. It was found that: (1) aperture width correlation length decreases with fracture surface roughness; (2) overall heat exchange efficiency increases with aperture width correlation length in the direction of flow; (3) Natural fracture apertures exhibit correlation length anisotropy which results in flow and heat exchange anisotropy. It is inferred that reduced aperture variability in the flow-parallel direction is favorable for the formation of strongly advective flow channels which thereby increase heat exchange. Partial upscaling of model results was accomplished via heat exchange analysis at elevated flow Peclet numbers within a static model geometry. It was found that for the case of laminar flow, surface roughness decreases heat exchange efficiency, with greater reduction at high flow velocity and Peclet number.

## 5.2. Future Work

Prediction of flow and heat exchange behaviors from morphological fracture characteristics remains a challenging and complex problem dependent upon a thorough understanding of the relevant physics, controlling parameters, and their relationships. While the findings of this work are consistent within a small sample size, further examination of the parameters controlling heat exchange should be conducted within a more extensive set of apertures. Acquisition of fracture surfaces from diverse rock types via white light profilometry for use in modeling could assist site-specific investigations of flow and heat or solute transport within a unit of interest.

While the three-dimensional Stokes equations provide a realistic and computationally feasible basis for modeling flow, the linear formulation of the equations cannot account for all aspects of flow which develop in nature. Notably, flow nonlinearities such as lee side eddies which develop around roughness protrusions are neglected. The effect of these features on flow, diffusive heat exchange and solute transport could be significant and should be investigated via further modeling with the full Navier-Stokes equations.

Lastly, further investigation of fracture aperture heterogeneity via geostatistical methods should be conducted with particular emphasis on the spatial distribution of asperities and their effect on flow. While it was found that asperity orientation relative to flow direction has a significant effect on hydraulic aperture, no geostatistical correlation was made and thus this topic should be considered for future work.

# Bibliography

- [1] Adler, P. M., & Thovert, J.-F. (1999). *Fractures and Fracture Networks* (1st ed.). Springer Netherlands. <https://doi.org/10.1007/978-94-017-1599-7>
- [2] Ivanova, V. M., Sousa, R., Murrihy, B., & Einstein, H. H. (2014). Mathematical algorithm development and parametric studies with the GEOFRAC three-dimensional stochastic model of natural rock fracture systems. *Computers and Geosciences*, 67(June), 100–109. <https://doi.org/10.1016/j.cageo.2013.12.004>
- [3] Wang, L., Cardenas, M. B., Slottke, D. T., Ketcham, R. A., & Sharp, J. M. (2015). Modification of the Local Cubic Law of fracture flow for weak inertia, tortuosity, and roughness. *Water Resources Research*, 51(4), 2064–2080. <https://doi.org/10.1002/2014WR015815>
- [4] Abdel-salam, A., & Chrysikopoulos, C. V. (1995). Analytical solutions for one-dimensional colloid transport in saturated fractures A. Abdel-Salam & C. V. Chrysikopoulos, Advances in Water Resources, 17(5), 1994, pp 283–296. *International Journal of Rock Mechanics and Mining Science & Geomechanics Abstracts*, 32(7), 318. [https://doi.org/10.1016/0148-9062\(95\)92365-O](https://doi.org/10.1016/0148-9062(95)92365-O)
- [5] D. H. TANG. (1981). Contaminant Transport in Fractured Porous Media: Analytical Solution for a Single Fracture. *Water Resources Research*, 17(3), 555–564. <https://doi.org/10.1016/j.cageo.2011.05.008>
- [6] Zou, L., Jing, L., Cvetkovic, V., Liangchao, B., & Se, Z. L. (2017). Modeling of Solute Transport in a 3D Rough-Walled Fracture-Matrix System. *Transport in Porous Media*, 116, 1005–1029. <https://doi.org/10.1007/s11242-016-0810-z>
- [7] Power, W. L., & Tullis, T. E. (1991). Euclidean and fractal models for the description of rock surface roughness. *Journal of Geophysical Research*, 96(B1), 415–424. <https://doi.org/10.1029/90JB02107>
- [8] Zambrano, M., Pitts, A. D., Salama, A., Volatili, T., Giorgioni, M., & Tondi, E. (2019). Analysis of fracture roughness control on permeability using SFM and fluid flow simulations: Implications for carbonate reservoir characterization. *Geofluids*, 2019. <https://doi.org/10.1155/2019/4132386>

- [9] Kosasih, W., & Rasouli, V. (2012). Geostatistical analysis of surface morphology and its relationship with hydro-mechanical properties of natural fractures. *WIT Transactions on Engineering Sciences*, 80, 209–219. <https://doi.org/10.2495/PMR120191>
- [10] Jacobs, T. D. B., Junge, T., & Pastewka, L. (2017). Quantitative characterization of surface topography using spectral analysis. *Surface Topography: Metrology and Properties*, 5(1). <https://doi.org/10.1088/2051-672X/aa51f8>
- [11] Brown, S. R., & Scholz, C. H. (1985). Broad bandwidth study of the topography of natural rock surfaces. *Journal of Geophysical Research*, 90(B14). <https://doi.org/10.1029/jb090ib14p12575>
- [12] Mandelbrot, B. B. (1983). *The Fractal Geometry of Nature* (1st editio). W. H. Freeman.
- [13] Ogilvie, S. R., Isakov, E., & Glover, P. W. J. (2006). Fluid flow through rough fractures in rocks. II: A new matching model for rough rock fractures. *Earth and Planetary Science Letters*, 241(3–4), 454–465. <https://doi.org/10.1016/j.epsl.2005.11.041>
- [14] Candela, T., Renard, F., Bouchon, M., Brouste, A., Marsan, D., Schmittbuhl, J., & Voisin, C. (2009). Characterization of fault roughness at various scales: Implications of three-dimensional high resolution topography measurements. *Pure and Applied Geophysics*, 166(10–11), 1817–1851. <https://doi.org/10.1007/s0024-009-0521-2>
- [15] Giacomini, A., Buzzi, O., Ferrero, A. M., Migliazza, M., & Giani, G. P. (2008). Numerical study of flow anisotropy within a single natural rock joint. *International Journal of Rock Mechanics and Mining Sciences*, 45(1), 47–58. <https://doi.org/10.1016/j.ijrmms.2007.04.007>
- [16] Witherspoon, P. A., Wang, J. S. Y., Iwai, K., & Gale, J. E. (1980). Validity of Cubic Law for fluid flow in a deformable rock fracture. *Water Resources Research*, 16(6), 1016–1024. <https://doi.org/10.1029/WR016i006p01016>
- [17] Piggott, R., & Elsworth, D. (1991). A hydromechanical representation of rock fractures. *32nd U.S. Symposium on Rock Mechanics*, 1165–1174.
- [18] Bear, J. (1972). *Dynamics of Fluids in Porous Media*. New York: American Elsevier Publishing Company.
- [19] Louis, C. (1969). *A study of groundwater flow in jointed rock and its influence on the stability of rock masses*. London.
- [20] Snow, D. T. (1965). A Parallel Plate Model of Fractured Permeable Media, 344. Retrieved from <http://search.proquest.com.ezproxy.library.ubc.ca/docview/30217-5868?accountid=14656>

- [21] Tsang, Y. W., & Sciences, E. (1984). The Effect of Tortuosity on Fluid Flow Through a Single Fracture, *20*(9), 1209–1215.
- [22] Milne-Thomson, L. (1968). *Theoretical Hydrodynamics: Fifth Edition* (5th ed.). Macmillan & Co Ltd 1968.
- [23] Pinkus, O., & Sternlicht, B. (1961). *Theory of hydrodynamic lubrication*. New York: McGraw-Hill Book Company Inc.
- [24] Brown, S. R. (1987). Fluid flow through rock joints: the effect of surface roughness. *Journal of Geophysical Research*, *92*(B2), 1337–1347. <https://doi.org/10.1029/JB092iB02p01337>
- [25] Brown, S. R., Stockman, H. W., & Reeves, S. J. (1995). Applicability of the Reynolds Equation for modeling fluid flow between rough surfaces. *Geophysical Research Letters*, *22*(18), 2537–2540. <https://doi.org/10.1029/95GL02666>
- [26] Zimmerman, R. W., Kumar, S., & Bodvarsson, G. S. (1991). Lubrication theory analysis of the permeability of rough-walled fractures. *High Level Radioactive Waste Management*, *28*(4), 535–541. [https://doi.org/10.1016/0148-9062\(92\)91194-a](https://doi.org/10.1016/0148-9062(92)91194-a)
- [27] Yeo, I. W., De Freitas, M. H., & Zimmerman, R. W. (1998). Effect of shear displacement on the aperture and permeability of a rock fracture. *International Journal of Rock Mechanics and Mining Sciences*, *35*(8), 1051–1070. [https://doi.org/10.1016/S0148-9062\(98\)00165-X](https://doi.org/10.1016/S0148-9062(98)00165-X)
- [28] Ge, S. (1997). A governing equation for fluid flow in rough fractures. *Water Resources Research*, *33*(1), 53–61. <https://doi.org/10.1029/96WR02588>
- [29] Brush, D. J., & Thomson, N. R. (2003). Fluid flow in synthetic rough-walled fractures: Navier-Stokes, Stokes, and local cubic law simulations. *Water Resources Research*, *39*(4). <https://doi.org/10.1029/2002WR001346>
- [30] Bodvarsson, G. (1969). On the Temperature of Water Flowing through Fractures, *74*(8), 14773–14792.
- [31] Bodvarsson, G. S., & Tsang, C. (1982). Injection and Thermal Breakthrough in Fractured Geothermal Reservoirs, *87*, 1031–1048.
- [32] Gringarten, A. C., & Sauty, J. P. (1975). A Theoretical Study of Heat Extraction From Aquifers With Uniform Regional Flow, *80*(35).
- [33] Li, W. (2014). Numerical and Analytical Modeling of Heat Transfer between Fluid and Fractured Rocks, *103*

- [34] Zhao, Z. (2014). On the heat transfer coefficient between rock fracture walls and flowing fluid. *Computers and Geotechnics*, 59, 105–111. <https://doi.org/10.1016/j.compgeo.2014-.03.002>
- [35] Sone, H., & Buob, M. (2018). Confining pressure dependence of roughness characteristics of granite fractures. *52nd U.S. Rock Mechanics/Geomechanics Symposium*.
- [36] Sarkar, S., Toksoz, M. N., & Burns, D. R. (2004). Fluid flow modeling in fractures. *Earth Resources Laboratory, MIT Earth*, 1–41.